Department of Physics and Astronomy

Heidelberg University

Master thesis in Physics

submitted by

Annabelle Valerie Kaiser

born in Villingen (Germany)

2022

Characterization of an ultra-stable voltage supply and implementation of sympathetic laser cooling for the $^3He^{2+}$ *g*-factor measurement

This Master thesis has been carried out by

Annabelle Valerie Kaiser at the

Max Planck Institute for Nuclear Physics

under the supervision of

Prof. Klaus Blaum and Dr. Andreas Mooser

Abstract:

The high-precision measurement of the nuclear g-factor of a single $^3He^{2+}$ stored in a Penning trap enables most accurate magnetometry using He nuclear magnetic resonance probes. The g-factor measurement requires the detection of an axial frequency shift caused by a spin flip. Due to the large mass and small magnetic moment of $^3He^{2+}$ compared to the proton and electron, this frequency shift is on the order of background frequency fluctuations, complicating the spin-state determination. The signal-to-noise ratio can be enhanced by implementing two upgrades to the Penning-trap setup. First, the electrode that generates the trap potential must be supplied with an ultra-stable voltage source that must be tunable in the range of a few hundred mV. At low electrode voltages ($\leq 500\,\mathrm{mV}$), the commercially available voltage source UM1-14 allows spin-flip detection with $99.2^{+0,4}_{-2,7}\%$ fidelity. However, for larger electrode voltages the UM1-14 is no longer suitable. Instead, a voltage source based on Josephson junctions was applied in the context of this thesis and gives a spin-flip detection fidelity of $98^{+1}_{-3}\%$. Second, the axial fluctuations are reduced by cooling the ion to low energies. This is achieved by sympathetic laser cooling of $^3He^{2+}$ coupled to laser cooled $^9Be^+$. After successful laser alignment, $^9Be^+$ was loaded into the trap and laser cooled. An upper limit of the achieved $^9Be^+$ axial temperature is presently at 4.2 K, which is far above the Doppler cooling limit of 0.5 mK.

Zusammenfassung:

Die Hochpräzisionsmessung des Kern-g-Faktors eines einzelnen, in einer Penning-Falle gespeicherten $^3He^{2+}$ ermöglicht extrem genaue Magnetometrie mittels He-Kernspinresonanz-Proben. Die g-Faktor Messung erfordert die Detektion einer axialen Frequenzverschiebung, hervorgerufen durch einen Spin-Flip. Aufgrund der großen Masse und des kleinen magnetischen Moments von $^3He^{2+}$ im Vergleich zum Proton oder Elektron liegt diese Frequenzverschiebung in der Größenordnung der Hintergrundfluktuationen, was die Bestimmung des Spin-Zustandes erschwert. Das Signal-Rausch-Verhältnis kann durch zwei Erweiterungen des Penning-Fallen-Aufbaus verbessert werden. Erstens benötigt die Elektrode, die das Fallenpotenzial erzeugt, eine ultrastabile und im Bereich von einigen hundert mV variable Spannungsversorgung. Bei niedrigen Elektrodenspannungen ($\leq 500\,\mathrm{mV}$) erreicht man mit der kommerziellen Spannungsquelle UM1-14 eine Spin-Flip-Detektionsgenauigkeit von $99.2^{+0,4}_{-2,7}\%$. Für größere Elektrodenspannungen wird die UM1-14 zu unstabil, weshalb im Rahmen dieser Arbeit eine Spannungsquelle basierend auf Josephson-Kontakten getestet wurde welche eine Spin-Flip-Detektionsgenauigkeit von $98^{+1}_{-3}\%$ ermöglicht. Zweitens werden die axialen Hintergrundfluktuationen durch Kühlung des Ions auf niedrige Energien reduziert. Dies wird durch die Kopplung von $^3He^{2+}$ an lasergekühltes $^9Be^+$ erreicht. Nach erfolgreicher Laserausrichtung wurde $^9Be^+$ in die Falle geladen und lasergekühlt. Eine Obergrenze der erreichten axialen Temperatur wurde zu 4.2 K bestimmt, welche weit über der Doppler-Kühlgrenze von 0.5 mK liegt.

Graphical abstract

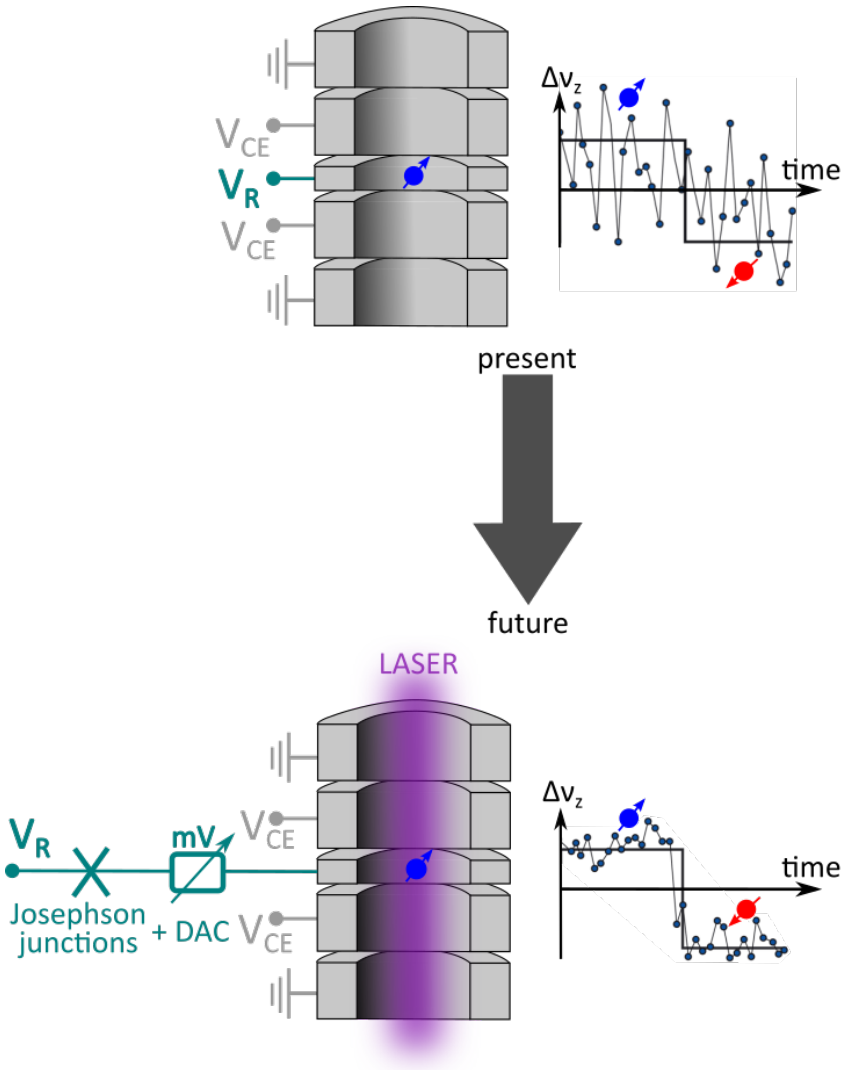

Contents

1 Introduction

The Standard Model of particle physics is currently the most comprehensive theory to describe the basic building blocks of the Universe: It classifies all elementary particles and explains how they interact and make up matter. The theory describes three of the four fundamental forces that govern the Universe: electromagnetic, weak and strong interactions, omitting gravity. Besides its powerful predictions e.g. in terms of the Higgs boson [ATLAS et al., 2012], it lacks to explain other phenomena like the non-zero masses of neutrinos or the matter-antimatter asymmetry.

To test the boundaries of theory, particles or particle interactions are studied at extremely high energy [Domènech et al., 2012], huge electric fields [Sturm et al., 2013] and at extremely high precision [Schneider et al., 2017, Smorra et al., 2017] in search for new physics beyond the Standard Model. One such example, namely the muon g-2 experiment at Fermilab and JPARC, is concerned with measuring the g-factor of the muon (or rather $g-2$) to a precision of 0.14 ppm [Jegerlehner, 2018]. The g-factor describes the ratio of the magnetic moment of a particle to its total angular momentum. Any significant deviation from the predicted theory value could be a sign for physics beyond the Standard Model, such as undiscovered particles. Within the experiment, a muon beam is transferred into an electromagnetic storage ring in which the muons travel around with immense velocity near the speed of light. The g-factor is determined from the precession of the muons' angular momentum in the magnetic storage field. To reach a high precision in the muon's g-factor, this magnetic field has to be known on the same level precision. Therefore, the B-field is calibrated in alternation with the muon g-factor measurements.

For absolute B-field calibrations, ^{3}He nuclear magnetic resonance (NMR) probes not only offer high precision but also high accuracy as required in the aforementioned experiment. Owing to it's noble gas properties, ^{3}He NMR probes need smaller corrections due to dependence on environmental impacts (e.g. temperature, pressure, impurities) than standard water or H_2 NMR probes [Nikiel et al., 2014]. For example, the needed correction due to temperature dependence of ^{3}He NMR probes is a hundred fold smaller than for water probes and the dependence on probe shape even reduces the systematics of ^{3}He NMR probes by a factor of one thousand as compared to water probes.

The shielded nuclear g-factor g_I' of $^3He^{1+}$ has only recently been measured with high accuracy to 0.25 ppb [Schneider et al., 2022], from which

the unshielded nuclear g-factor g_I can be extracted with a precision of 1 ppb using quantum electrodynamics (QED) theory - one of the most important fundamental theories of the Standard Model. The diamagnetic shielding refers to the electron surrounding the nucleus, which has a magnetic moment itself and therefore slightly reduces the coupling of the nuclear magnetic moment to an external magnetic field [Rudziński et al., 2009]. The direct high-precision measurement of the unshielded nuclear g-factor g_I is the next important step to establish ^{3}He as a robust NMR probe for accurate magnetometry. Moreover, this measurement opens the possibility to test bound-state QED theory by comparing the bound state g-factor g'_I of a nucleus to the bare g-factor g_I of the same nucleus.

The ^{3}He-experiment located at the Max Planck Institute for Nuclear Physics in Heidelberg is dedicated to perform the first direct measurement of the helion's ($^3He^{2+}$) nuclear g-factor. Using a cryogenic Penning-trap setup, in which a single $^3He^{2+}$ can be trapped for months by a superposition of a magnetic field and an electrostatic potential, a precision of 1 ppb or better can be reached [Schneider et al., 2022]. Within such an electromagnetic field, the ion's motion consists of one axial eigenmotion (along the magnetic field lines) and two radial eigenmotions (perpendicular to the magnetic field lines) called the modified cyclotron and the mangetron motion. For the g-factor measurement, the spin-state of the ion has to be determined in a trap with an inhomogeneous B-field, via the so-called continuous Stern-Gerlach effect [Dehmelt, 1986]. In such a field, a spin-flip induces a shift in the ion's axial frequency which has to be resolved. Compared to the proton [Mooser et al., 2014, Schneider et al., 2017] or antiproton [Smorra et al., 2017], whose g-factors have already been successfully determined in a Penning trap, the helion's larger mass and smaller magnetic moment lead to a three times smaller axial frequency shift between the spin-up and the spin-down state. In the case of the helion, the axial frequency shift caused by a spin-flip is of the order of the background fluctuations. Hence, for resolving the spin-flip and enabling the nuclear g-factor measurement, these background fluctuations have to be reduced.

This challenge is met by implementing two upgrades into the Penning-trap setup: The first makes use of an ultra-stable voltage source which is applied to the electrode creating the electrostatic potential in the Penning trap, in which the spin-flip is determined. The smaller the noise of the voltage which is applied to this electrode, the smaller the noise in the axial mode of the ion's motion.

Another major contribution to fluctuations in the axial mode arises from random quantum jumps in the ion's modified cyclotron mode, which is coupled to the axial mode in an inhomogeneous B-field. The modified cyclotron frequency (and hence energy) is usually a few orders of magnitude larger than the axial frequency. Therefore, random quantum jumps are much more

likely to occur. Every quantum jump in the modified cyclotron mode induces a shift in the axial frequency. By decreasing the helion's energy in the modified cyclotron mode, this noise contribution is reduced. Extremely low energies can be reached with laser cooling the ion. As $^3He^{2+}$ does not have a laser cooling transition itself, another ion species ($^9Be^+$) will be laser cooled while being coupled to the helion. Through energy exchange, the helion is sympathetically cooled. Sympathetic laser cooling in a Penning trap for two spatially separated ion species was first demonstrated in 2021 [Bohman et al., 2021, Tu et al., 2021] for a proton and laser cooled beryllium ions. The method is extremely powerful, as it can in principle be applied to any ion without a laser cooling transition, such as $^3He^{2+}$. Both upgrades were examined within this project.

In this work, the theoretical and experimental requirements that enable nuclear spin-flip detection of $^3He^{2+}$ are treated. Chapter 2 gives an introduction to the basic principles of Penning traps and the g-factor determination within the Penning trap. The required voltage stability to observe spin flips with a fidelity of 99 % is calculated as teaser for Chapter 3. Here, the framework for supplying the Penning-trap electrodes with an ultra-stable voltage supply is set and the performance of this voltage source is characterized. Chapter 4 deals with the second part of facilitating the spin-flip detection: the implementation of sympathetic laser cooling. Foremost, Chapter 4 treats the $^9Be^+$ laser cooling transitions in a strong magnetic field, the laser setup used to cool beryllium ions and the temperature measurement of a cloud of trapped beryllium ions. At last, the respective results are discussed in Chapter 5 and a short outlook is given.

2 The Penning trap

To perform high-precision measurements on single charged particles, so-called Penning traps can be used [Blaum, 2006, Brown and Gabrielse, 1986]. These traps allow the characterization of different properties of charged particles, such as their mass, the magnetic moment of the bound electron or even the nuclear magnetic moment of the proton and the antiproton [Ulmer et al., 2016, Schneider et al., 2017, Smorra et al., 2017]. The latter will be treated in the scope of this thesis for heavier species like the helion. In this section, a basic introduction to Penning traps will be given and the methods used for high-precision measurements of the nuclear magnetic moment of single charged particles are described.

2.1 Trapping potentials

In a Penning trap, a charged particle is stored in three dimensions by superimposing a homogeneous magnetic field $\vec{B} = B_0\vec{e_z}$ with an electrostatic quadrupole potential Φ. The magnetic field confines a particle of charge q and mass m in radial direction ρ, given in cylindrical coordinates $\rho^2 = x^2 + y^2$, by forcing it onto a circular trajectory with the free-space cyclotron frequency

$$\omega_c = \frac{q}{m}B_0. \tag{2.1}$$

The trapping in z-direction is achieved by a weak electrostatic quadrupole potential

$$\Phi(z,\rho) = V_R C_2 \left(z^2 - \frac{1}{2}\rho^2\right), \tag{2.2}$$

where V_R is the potential applied to the ring electrode relative to the endcap potential, C_2 is a geometric parameter and $z = \rho = 0$ determines the center of the trap. This electrostatic potential is reproduced by hyperbolic electrodes. In modern Penning-trap experiments, a stack of cylindrical trap electrodes is used instead, see Figure 2.1a. The stack produces a symmetric and nearly perfect quadrupole-like potential near the center of the trap [Gabrielse et al., 1989], which can be expanded as

$$\Phi(z) = V_R \sum_n C_{2n} z^{2n} = V_R \left(C_2 z^2 + C_4 z^4 + C_6 z^6 + ...\right). \tag{2.3}$$

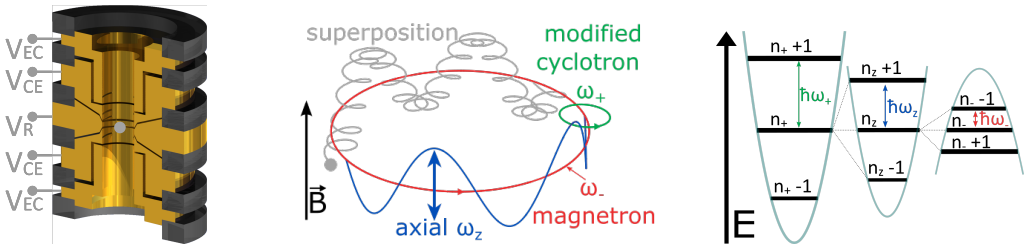

(a) (b) (c)

Figure 2.1: Penning-trap basics. (a) Design of a cylindrical five pole Penning trap and (b) trajectory of a trapped ion, which consists of three decoupled eigenmotions referred to as axial, magnetron and modified cyclotron motion. (c) Equivalent energy levels of a single particle in a Penning trap. The distances between the levels of the different modes are not to scale.

Correction electrodes with the potential V_{CE} are placed next to the central ring electrode. The electrode lengths and radii can be designed such that for an optimized tuning ratio $TR = V_{\mathrm{CE}}/V_R$, the axial frequency of the ion becomes independent of V_{CE} and simultaneously, the higher order corrections C_4 and C_6 of the multipolar expansion are tuned to zero. A Penning trap meeting these conditions is said to be *orthogonal* and *compensated*.

2.2 Eigenfrequencies of trapped ions

Within this electromagnetic field, the trajectory of a trapped particle is composed of three eigenmotions (compare Figure 2.1b, 2.1c), behaving like decoupled harmonic oscillators with the characteristic eigenfrequencies

$$\omega_z = \sqrt{2\frac{q}{m}V_R C_2} \quad \text{and} \quad \omega_\pm = \frac{\omega_c}{2} \pm \sqrt{\frac{\omega_c^2}{4} - \frac{\omega_z^2}{2}}. \tag{2.4}$$

The axial motion with frequency ω_z occurs along the magnetic field lines whereas the motion in radial plane consists of a rapid modified cyclotron frequency ω_+ and a slow magnetron frequency ω_-. As trapping criterion, the magnetic field has to be large enough with respect to the electrostatic potential, satisfying $\omega_c^2 > 2\omega_z^2$. Therefore, the typical eigenfrequency hierarchy obeys $\omega_+ > \omega_z > \omega_-$ [Blaum, 2006].

The eigenfrequencies are measured using a resonator circuit: The up and down movement of the ion within the trap induces image charge currents in the outer electrode at exactly ω_z. This current is detected by a resonator circuit in parallel to the ion. When the ion is at thermal equilibrium with the resonator, it shorts the noise of the resonator and a noise dip appears at the axial frequency of the ion in the FFT spectrum (*fast Fourier transform*

spectrum). Such a noise dip signal, indicating trapped ions, and a schematic resonator are illustrated in Figure 2.2. The width of the dip signal scales linearly with the number of trapped ions. To increase the signal amplitude, amplifiers are placed behind the resonator. The magnetron and modified cyclotron frequency are obtained by coupling each mode to the axial frequency using the lower sideband. Doing so, a double dip appears in the FFT spectrum, from which the two eigenfrequencies can be extracted.

The free-space cyclotron frequency is obtained from the eigenfrequencies within the trap, either by using the sideband relation

$$\omega_c = \omega_+ + \omega_-, \tag{2.5}$$

which is often used in on-line mass spectrometry experiments dealing with short-lived nuclei, or by means of the Brown Gabrielse invariance theorem [Brown and Gabrielse, 1982]

$$\omega_c^2 = \omega_+^2 + \omega_z^2 + \omega_-^2, \tag{2.6}$$

which is used in high-precision measurements, as Equation (2.6) is robust against typical first order trap imperfections [Gabrielse, 2009]. Such imperfections are for example

- a tilt of the axis of the magnetic field relative to the symmetry axis of the trap electrodes or
- slight ellipticities of the quadrupole potential.

Other deviations from the ideal Penning trap include octupolar and hexapolar modifications of the electrostatic trapping potential $C_4 z^4 + C_6 z^6$ (this can be compensated by implementing additional electrodes next to the central ring electrode as discussed in the previous section) and a slightly inhomogeneous magnetic field $B_z = B_0 + B_2 z^2$, which has to be characterized by measurements. Relativistic effects, frequency shifts induced by image charge- and detector interactions or other effects modifying the eigenfrequencies also have to be considered. However, a detailed discussion is beyond the scope of this thesis and can be found in full glory in [Brown and Gabrielse, 1986].

Penning-trap experiments built for high-precision measurements consist of some basic ingredients, which are among others:

- a set of trap electrodes of cylindrical (or hyperbolic) geometry, situated in
- a very homogeneous, superconducting magnet of high field strength (B_0 of a few T) and
- a cryogenic environment,

- highly stable dc power supplies,
- radio frequency (rf) electronics and
- superconductive low-noise electronics.

In order to improve the present best limit set by the experiment described here [Schneider et al., 2017] further technical improvements are needed. Two such upgrades are a highly stable voltage supply based on Josephson junctions to improve the stability of the ion's axial motion in the Penning trap as well as sympathetic laser cooling to decrease the helion's temperature. These two developments are the content of this thesis and will be discussed in chapter 3 and 4, respectively.

2.3 *g*-factor measurement

The helium ion $^3He^{2+}$ has a nuclear spin $I = 1/2$ and an associated magnetic moment

$$\vec{\mu_I} = g_{He}\mu_N\vec{I} \quad \text{with} \quad \mu_N = \frac{e\hbar}{2m_p}, \tag{2.7}$$

where g_{He} denotes the nuclear g-factor and μ_N the nuclear magneton. In a magnetic field, the two possible spin-states $m_I = \pm 1/2$ are separated by an energy difference

$$\hbar\omega_L = 2\mu_I B_0 = g_{He}\mu_N B_0, \tag{2.8}$$

with ω_L being the Larmor frequency. By taking the ratio of the Larmor frequency and the free cyclotron frequency, the B-field dependency drops out, and the g-factor is given by

$$\frac{\omega_L}{\omega_C} = g_{He}\frac{m_{He}}{4m_p}. \tag{2.9}$$

The helion-to-proton mass ratio is well known to 50 ppt [CODATA, 2022]. The Larmor and free cyclotron frequency have to be obtained experimentally in order to determine the nuclear g-factor. Different Penning traps are used for these measurements, as illustrated in Figure 2.2. Why multiple traps are necessary is discussed below.

As stated previously, the **free cyclotron frequency** is derived from the invariance theorem (Eq. 2.6). Therefore, the three eigenfrequencies $\omega_\pm$ and ω_z are measured to high precision in the so-called *precision trap* (compare Fig. 2.2).

For the determination of the **Larmor frequency**, the energy splitting between the spin-states is probed using the continuous Stern-Gerlach effect

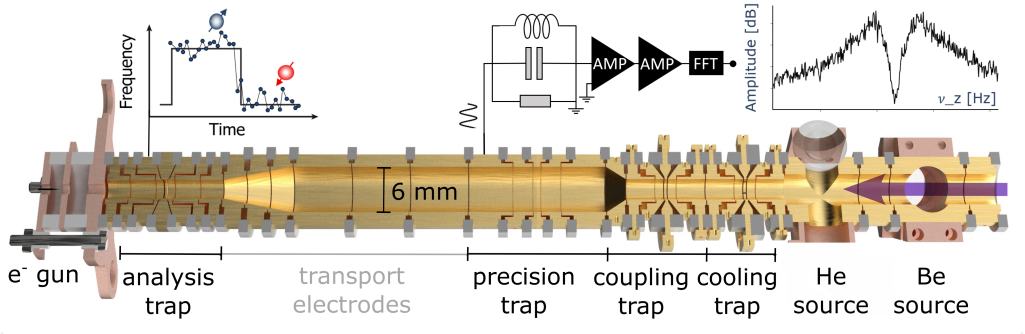

Figure 2.2: Penning trap assembly as planned for the nuclear g-factor measurement of $^3He^{2+}$. Beryllium produced by laser ablation from the Be source is trapped and laser-cooled in the cooling trap. The cooling-laser goes straight through the trap tower. Helium produced from the He source and ionized by the e^- gun is sympathetically laser-cooled in the coupling trap. Once cooled, the eigenfrequencies and the spin-state are determined in the precision trap and the analysis trap, respectively. The inset above the analysis trap shows a hypothetical spin-flip signal (left). The resonator circuit (middle) connected to the precision trap is used to detect the ion and determine it's eigenfrequencies from the dip signal in the FFT (right).

[Dehmelt, 1986]. This is done in the *analysis trap* (Fig. 2.2), which has an inhomogeneous B-field (a so-called magnetic bottle $B_z = B_0 + B_2 z^2$). As a result, a spin-flip of the helium nucleus shifts the axial frequency by

$$\Delta\nu_{z,SF} = \frac{B_2 \mu_I}{2\pi^2 m_{He} \nu_z}. \tag{2.10}$$

The ferromagnetic correction electrodes creating such a magnetic bottle and a schematic spin-flip is illustrated in Figure 2.3. Observing this frequency shift, which indicates a spin quantum jump, is crucial, as the Larmor frequency can be extracted from a measurement of spin-flip probability over spin-flip drive frequency [Mooser et al., 2018]. However, in the case of $^3He^{2+}$, this axial frequency shift is approximately 100 mHz and has to be resolved on top of a typical axial frequency of 700 kHz. This becomes difficult in a noisy environment.

Difficulty of spin-state detection:

A strong B-field inhomogeneity B_2 is desired, as it increases the axial frequency shift induced by a spin-flip $\Delta\nu_{z,SF}$ (Eq. (2.10)). At the same time, a large B_2 increases the coupling between the cyclotron mode energy E_+

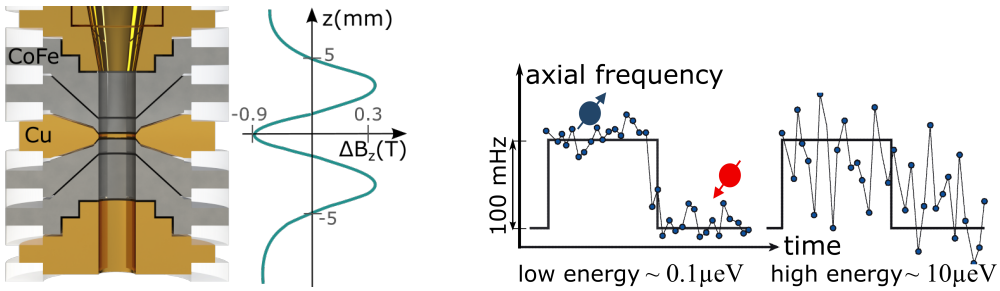

(a) (b)

Figure 2.3: Spin-state detection occurs in the analysis trap. (a) The ferromagnetic correction electrodes create a B-field inhomogeneity on top of the homogeneous magnetic field of 5.7 T. This inhomogeneity B_2 couples the spin-state of the helion to its axial frequency ν_z. (b) A spin-flip results in an axial frequency jump $\Delta\nu_{z,SF}$ of approximately 100 mHz in the case of $^3He^{2+}$. For high particle energies and noisy voltage supplies, the fluctuations in ν_z are of the order of the frequency jump caused by a spin-flip.

and the axial mode

$$\Delta\nu_z \simeq \frac{1}{4\pi^2 m_{He}\nu_z}\frac{B_2}{B_0}\left(E_+ + |E_-| \pm \mu_I B_0\right) \quad \text{[Mooser et al., 2013]}, \quad (2.11)$$

and thus, random cyclotron quantum jumps are visible in the axial mode as noise. These quantum jumps $\partial n_+/\partial t \propto E_+$ increase with the cyclotron energy E_+ [Mooser et al., 2013, 2018], which is illustrated in Figure 2.4a. Therefore, spin-state detection can be facilitated by **sympathetically laser cooling the ion**, to reduce it's cyclotron energy. With sympathetic laser cooling, cyclotron temperatures in the mK range can be reached, whereas resistive cooling is limited to the resonators minimal temperature of 4 K. Sympathetic laser cooling therefore increases the spin-flip detection fidelity by about 40 % with respect to resistive cooling (see Fig. 2.4b). However, it can be seen from Figure 2.4a that even at zero cyclotron energy, the frequency fluctuations in the axial mode do not drop to zero. This offset is caused by noise induced from the voltage source.

A spin-flip $\Delta\nu_{z,SF}$ can only be detected for a sufficiently stable axial frequency ν_z (Eq. (2.10)). As the axial frequency depends on the voltage applied to the ring electrode V_R (Eq. (2.4)), a voltage source with low electronic noise and low drift is desirable. This issue is addressed by **supplying the central ring electrode with an ultra-stable and low drift voltage source**. The offset in Figure 2.4a can thus be minimized.

The first subject is treated in the following chapter 3, the latter will be regarded in chapter 4.

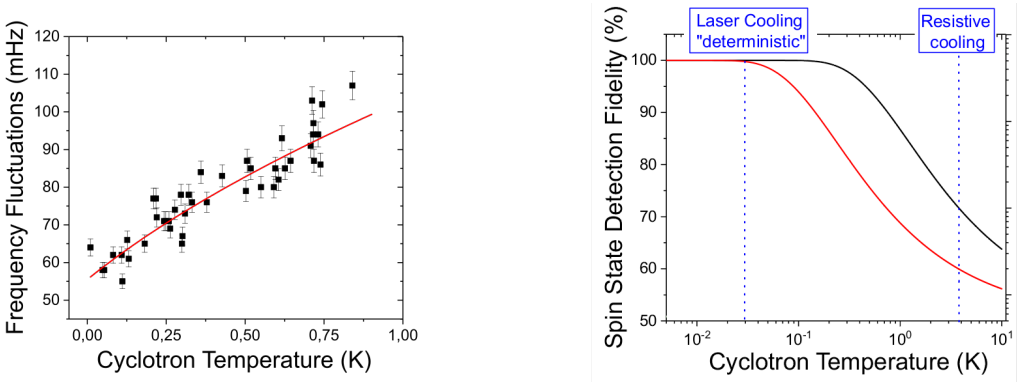

(a) (b)

Figure 2.4: Spin-state detection fidelity. (a) The random quantum jumps in the cyclotron mode increase with the cyclotron energy $E_+ \propto T_+$. Due to the coupling between axial and cyclotron mode in an inhomogeneous B-field, these quantum jumps are visible in the axial mode as frequency fluctuations. (b) When the helion (red curve) is in thermal equilibrium with the resonator, the spin-state is detected with a fidelity of roughly 60 %. Cooling the cyclotron mode with a laser increases the detection fidelity to almost 100 %. The proton (black curve) has a smaller mass and larger magnetic moment, which increases the axial frequency shift caused by a spin-flip. Hence, the spin-state is detected with more certainty than in the case of the helion for a fixed temperature. Pictures adapted from [Mooser et al., 2018].

2.4 Required voltage stability for the helion *g*-factor measurement

The voltage stability on the electrodes of the analysis trap required to resolve a single helion spin-flip will be estimated in this section. The analysis trap consists of five electrodes, of which the outer two, the endcaps, are on ground potential. The ring electrode is located in the center of the trap, enclosed by the two correction electrodes (compare Fig. 2.1a). The trapped particle reacts most strongly to the noise of the ring electrode, since it generates the potential that the particle senses. In an ideal orthogonal trap, the motion of the ion is independent of the potential applied to the correction electrodes. However, experimental reality shows that the voltage on the correction electrodes has a small residual influence on the particle.

Nevertheless, the required voltage stability on the ring electrode is higher than on the correction electrodes. Hence, the ring and correction electrodes and their respective noise limits will be treated separately.

	q (e)	m (u)	μ_I (μ_N)	ν_z (kHz)	$\Delta\nu_{z,SF}$ (mHz)
$^3He^{2+}$	2	3.014	-2.128	700	**100**
p	1	1.007	2.793	860	**320**

Table 2.1: Axial frequency ν_z and frequency jump caused by a spin-flip $\Delta\nu_{z,SF}$ of a helion or proton, as expected in the analysis trap of the experiment. For calculating ν_z and $\Delta\nu_{z,SF}$, the values $B_2 = -646.4\,\mathrm{kT\,m^{-2}}$, $V_R = -0.43\,\mathrm{V}$ and $C_2 = 350\,000\,\mathrm{m^{-2}}$ were used. Particle properties were obtained from the Committee on Data for Science and Technology [CODATA, 2022].

Noise limit on the ring electrode:

The spin-flip induced frequency shift in the axial mode $\Delta\nu_{z,SF}$ is dependent on particle properties (such as the charge q_{He}, mass m_{He}, and magnetic moment μ_I) as well as on experimental conditions (like the B-field inhomogeneity B_2, the applied ring voltage V_R and the trap geometry C_2), compare Equations (2.10), (2.7) and (2.4). By choosing $^3He^{2+}$ for the measurement, the particle properties become fixed, see Table 2.1. The experiment is designed for realizing a helion nuclear g-factor measurement, providing the remaining parameters $B_2 = -646.4\,\mathrm{kT\,m^{-2}}$ [Schneider, 2019], $V_R = -0.43\,\mathrm{V}$ and $C_2 = 350\,000\,\mathrm{m^{-2}}$.

Compared to the proton g-factor, which was already measured to high precision using a Penning-trap setup [Mooser et al., 2014, Schneider et al., 2017], the helion's larger mass, charge and smaller magnetic moment decreases $\Delta\nu_{z,SF}$ by a factor of three, shown in Table 2.1 (Eq. (2.10)). This makes the identification of a spin-flip much harder.

For the determination of the Larmor frequency, a series of axial frequency measurements $\nu_{z,i}$ is taken, between which spin-flips are driven. The overall distribution of axial frequency fluctuations between two consecutive measurements $\Delta\nu_{z,i} = \nu_{z,i} - \nu_{z,i+1}$ can be described by three separate, non-independent normal distributions with standard deviation σ_z: the background fluctuations not containing any spin-flips (mean value $\mu = 0$) superimposed by fluctuations from spin down to spin up and vice versa (mean value $\mu = \pm\Delta\nu_{z,SF}$) [Mooser, 2014]. This is illustrated in Figure 2.5.

To identify a single spin-flip, a threshold TH can be introduced, and interpreted as follows:

$$\begin{aligned} \Delta\nu_{z,i} &\geq TH \Rightarrow \text{spin-flip from up to down,} \\ \left|\Delta\nu_{z,i}\right| &\leq TH \Rightarrow \text{no spin-flip,} \\ -\Delta\nu_{z,i} &\geq TH \Rightarrow \text{spin-flip from down to up.} \end{aligned}$$

The optimum spin-flip fidelity depends on the chosen threshold TH, which in turn depends on the scale of the frequency fluctuations in the

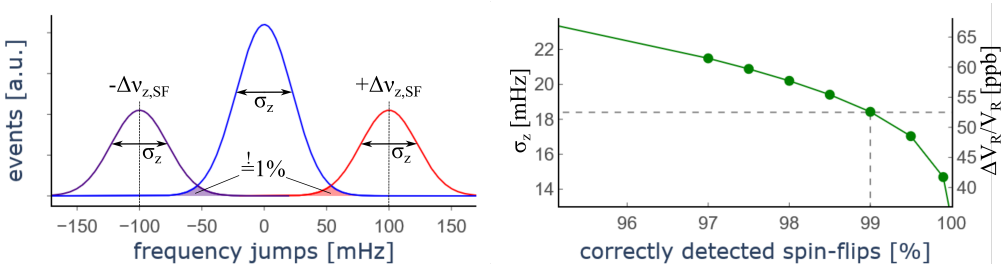

Figure 2.5: Spin-flip detection statistics. (a) Theoretical distribution of axial frequency fluctuations $\Delta\nu_{z,i}$ with standard deviation σ_z and the mean values 0 and $\pm\Delta\nu_{z,SF}$. Blue shows the background fluctuations, not containing any spin-flips, red and indigo show the frequency shifts due to spin-flips. Background fluctuations that are misinterpreted as spin-flips and spin-flips that are assigned to background fluctuations are located in the overlapping region between the two neighbouring curves (shaded red and indigo). For detecting a spin-flip correctly with a probability of 99 %, this area has to be 1 % of the total area below the spin-flip curve. (b) Limit on frequency fluctuations σ_z and associated relative voltage stability $\Delta V_R/V_R$ of the voltage supply for different spin-flip fidelities. At 99 %, the required relative voltage stability is below 53 ppb. The total axial frequency used in the calculation is $\nu_z = 700\,\mathrm{kHz}$ (Eq. (2.13)).

axial mode. For small fluctuations, the ideal threshold that maximizes the spin-flip fidelity converges to $TH = \Delta\nu_{z,SF}/2$ [Mooser, 2014].

To detect a spin-flip induced frequency jump with a fidelity of 99 %, the overlapping area between background fluctuations and spin-flips has to be 1 % of the total spin-flip area, as illustrated in Figure 2.5. The upper limit on allowed frequency fluctuations in the axial mode σ_z is obtained from integrating over this area:

$$\frac{1}{16\sqrt{2\pi}\sigma_z}\left[\int_{-\infty}^{TH}\exp\left(-\frac{(\nu-\Delta\nu_{z,SF})^2}{2\sigma_z^2}\right)d\nu+\int_{TH}^{\infty}2\exp\left(-\frac{\nu^2}{2\sigma_z^2}\right)d\nu\right]\stackrel{!}{=}1\,\%. \tag{2.12}$$

In a Penning trap, the axial frequency is directly related to the potential applied to the ring electrode. The needed frequency stability therefore gives constrains on the voltage source that can be used for supplying the central ring electrode. Differentiating the equation for the axial eigenfrequency (Eq. (2.4)) with respect to the ring voltage yields:

$$\Delta\nu_z = \frac{1}{2\pi}\sqrt{\frac{qC_2}{2mV_R}}\Delta V_R \quad\Rightarrow\quad \frac{\Delta V_R}{V_R} = 2\frac{\Delta\nu_z}{\nu_z} \tag{2.13}$$

Hence, using the values from Table 2.1 with the given threshold of $TH = \Delta\nu_{z,SF}/2$, the relative voltage has to be stable on a level of 53 ppb within the measurement time of approximately two minutes.

Noise limit on the correction electrodes:

For quantifying the needed voltage stability on the correction electrodes, the parameter D_2 is crucial:

$$D_2 = \frac{\partial\nu_z}{\partial TR} = \frac{\nu_z}{2V_R}\frac{\partial V_R}{\partial TR}, \quad [D_2] = \frac{\mathrm{mV}}{\mathrm{mU}}. \tag{2.14}$$

D_2 describes the amount of orthogonality in the trap, such that $D_2 = 0$ corresponds to a trapped particle, whose axial frequency is independent of the voltage applied to the correction electrodes. In the analysis trap used for the helion g-factor measurement, this parameter was experimentally determined by S. Dickopf to be $D_{2,exp} = 0.024\,\mathrm{mV\,mU^{-1}}$. The milli-unit mU describes the change of the dimensionless tuning ratio $TR = V_{\mathrm{CE}}/V_R$ by 10^{-3}. The voltage can be associated with a frequency, again by using Equation (2.13). Dividing the D_2 parameter by the ring voltage V_R yields a conversion ratio from noise in the correction electrode voltage to frequency fluctuations of the particle. To detect a single spin-flip, the noise limit of the voltage source is determined by

$$\Delta V_{CE} = \frac{V_R}{D_{2,exp}}\frac{\delta\nu_z}{\Delta\nu_z(\Delta V_R = 1\,\mathrm{mV})}. \tag{2.15}$$

Using the values from above ($\sigma_z = \Delta\nu_{z,SF}/2 = 23\,\mathrm{mHz}$, $V_R = -0.43\,\mathrm{V}$, $C_2 = 350\,000\,\mathrm{m^{-2}}$ and $D_{2,exp} = 0.024\,\mathrm{mV\,mU^{-1}}$) determines the upper noise limit of the correction electrodes at 0.51 µV, or relative to the ring voltage at 1.2 ppm.

In summary, the ring electrode requires a voltage supply with higher stability of the order of 53 ppb, while a stability of about 1.2 ppm is sufficient for the correction electrodes within the measurement time of approximately two minutes. Taking into account, that the voltage applied to the ring electrode of the analysis trap will be around $V_R = -0.43\,\mathrm{V}$, this gives the absolute noise limits of 23 nV and 0.51 µV for ring and correction electrode, respectively. With these stability limits, a spin-flip is correctly detected with a probability of 99 %.

3 Josephson voltage source

The spin-state determination of $^3He^{2+}$ is the most important step for the helion nuclear g-factor measurement. As mentioned in section 2.4, a spin-flip is observed by a shift in the axial frequency due to the coupling of the spin magnetic moment and the axial mode in the magnetic bottle. However, this observation becomes difficult in a noisy environment (compare Fig. 2.3b). Especially, electronic noise from the voltage sources connected to the trap electrodes leads to noise in the axial frequency. To distinguish the axial frequency shift caused by a spin-flip from other frequency fluctuations, the electronic noise has to be sufficiently low. This motivates the implementation of an ultra-stable voltage source based on Josephson junctions in the experiment. For simplicity, such a voltage source will be called *Josephson voltage source* from now on.

The stability requirements for such a voltage source have been discussed in the previous section. Now, we will examine how well this Josephson voltage source meets our necessities with respect to stability and tunability. After an introduction to the working principles of Josephson junction based voltage sources, the operational setup will be introduced. The different possibilities for tuning a Josephson voltage source are discussed and at last, the results of the voltage stability measurements are presented.

3.1 Josephson junctions

The Josephson junction dates back to 1962, when the Cambridge University student Brian Josephson derived equations for the current-voltage characteristics across a so-called Josephson junction [Josephson, 1962]. Such a junction consists of two superconductors separated by a thin insulating or normal conducting layer (compare Fig. 3.1a). Cooper pair tunneling through the barrier leads to two effects: the dc and the ac Josephson effect. The dc Josephson effect describes that at zero voltage, a dc supercurrent can flow across the junction. The ac Josephson effect predicts that if a voltage V is applied across the junction, an ac supercurrent of frequency $f_J = (2e/h)V$ is added to the dc supercurrent, where h is Planck's constant and e is the elementary charge. By applying an external signal with frequency f, this oscillation can be phase locked leading to steps of constant voltage:

$$V_n = \frac{nh}{2e} f = \frac{n}{K_J} f, \quad K_J = 483\,597.8484\,\mathrm{GHz\,V^{-1}} \quad \text{[CODATA, 2022]},$$

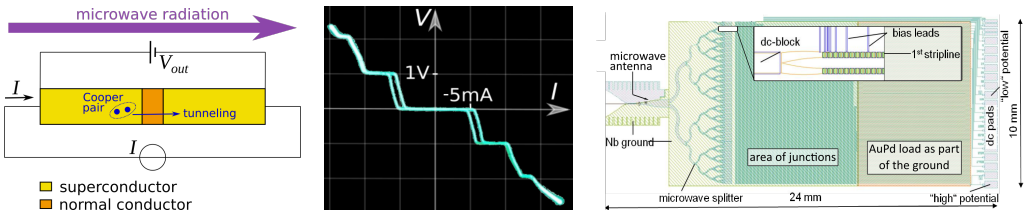

(a) (b) (c)

Figure 3.1: Josephson junction working principle and schematic layout of a Josephson voltage source. (a) A Josephson junction consists of two superconductors (Nb) separated by a thin normal conducting layer (Nb_xSi_{1-x} with $x \approx 10\,\%$). By applying microwave radiation across the junction, the output voltage becomes quantized. (b) The characteristic voltage-current curve of a Josephson junction shows non-ohmic behaviour with steps of constant voltage. The hysteresic parts in the oscilloscope picture vanish for dc currents (the ac currents have to be applied in order to picture the whole curve). (c) Schematic Josephson junction array as fabricated at the *Physikalisch Technische Bundesanstalt* (PTB) [Müller et al., 2014, Kohlmann and Behr, 2011]. The microwave radiation is split and equally distributed across the striplines containing the Josephson junctions. Before the dc readout pads, the remaining microwave radiation is absorbed by a AuPd load.

(3.1)

with the Josephson constant K_J. The output voltage only depends on the applied frequency, the step number n and fundamental constants. Therefore, such systems represent perfect frequency-to-voltage converters and are nowadays used in metrology as the basis for voltage standards [Behr et al., 2012], considering that the second becomes directly related to the voltage (Eq. 3.1).

This phenomenon, which is known as the *inverse ac Josephson effect*, was experimentally confirmed a year later by Sidney Shapiro [Shapiro, 1963] and therefore the regions of constant voltage are also known as Shapiro steps, with number n. The characteristic current-voltage curve of such a Josephson junction is illustrated in Figure 3.1b. For a current around zero, the zeroth Shapiro step has an output voltage of $V = 0$. Only if a threshold current is overcome, the absolute voltage across the junction is greater than zero with its value being determined by the applied frequency f and -depending on the current- the number of Shapiro steps. It is obvious from the plot, that a current source with some noise ΔI does not affect the output voltage of the junction, as long as the current $I \pm \Delta I$ never leaves the Shapiro step.

number of junctions	N	8192
frequency range	f	68.7 GHz to 72.9 GHz
critical current	I_c	6.4 mA
width of 0^{th} step	ΔI_0	$\sim$ 4.0 mA (at 70 GHz)
width of 1^{st} step	ΔI_1	$\sim$ 2.5 mA (at 70 GHz)
maximum voltage on 1^{st} step	V_{max}	1.235 V

Table 3.1: The Josephson voltage source provided for the helion g-factor measurement.

The voltage applied to the ring electrode in the analysis trap is around $-0.43\,\text{V}$. To reach such a voltage, many junctions have to be put into series. Following Kirchhoff's second law [Kirchhoff, 1845], Equation (3.1) is modified to

$$V_{n,N} = N\frac{n}{K_J}f, \tag{3.2}$$

with the total number of junctions in series N. All junctions are placed on a chip in multiple striplines as illustrated in Figure 3.1c [Müller et al., 2014]. The microwaves are distributed equally across the Josephson junction array and are absorbed behind the array.

3.2 Operating a Josephson voltage source

The Josephson effect evolves from superconductivity. Accordingly, Josephson junctions are operated in a cryogenic environment. By radiating microwaves across the junctions, the output voltage becomes quantized. At last, a current is applied to the array of junctions.

Ideally, a current in the center of a Shapiro step is chosen. In that case, fluctuations of the supplying current source smaller than half the step width will have no influence on the output voltage. A schematic layout of an operational setup is illustrated in Figure 3.2a.

The Josephson array intended for the helion g-factor measurement was kindly provided by R. Behr and L. Palafox from the *Physikalisch Technische Bundesanstalt* along with all other tools required for operating a Josephson voltage source. A picture of the used setup and Josephson voltage source is provided in Figure 3.2. Table 3.1 gives technical details of the used array, more details on the operation can be found in the appendix B.1.

Besides having an ultra-stable voltage supply, another requirement for the g-factor measurement is the tunability of the voltage source. Trapping potentials have to be changed for transporting the ion between different traps and the theoretical predictions for the required potential on the electrodes might deviate from the experimental reality. Several options exist for

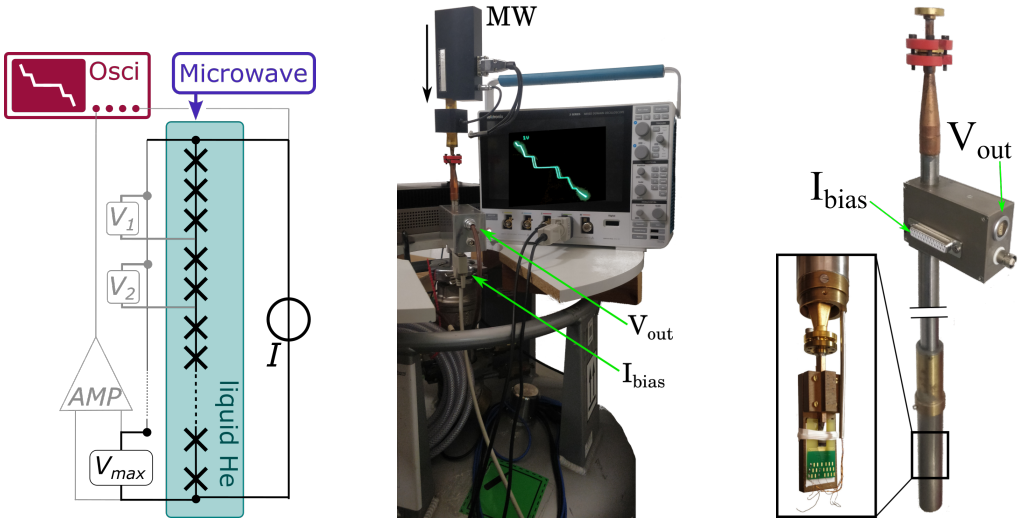

(a) (b) (c)

Figure 3.2: Setup for operating a Josephson voltage source. (a) The Josephson junctions (illustrated as crosses) are placed in a cryogenic liquid helium tank (temperature of roughly 4 K). Microwaves are irradiated across the array via a microwave guide. The voltage can be read out from the entire array V_{max} or from parts of the array V_i. (b) The optimal current is found by displaying the current-voltage curve on an oscilloscope and choosing the center of a Shapiro step. The electrical leads for the bias current and the output voltage are connected to the top of a 1 m long rod, which is inserted into the liquid helium dewar. (c) Inside the rod, the microwave guide and twisted copper cables are led to the Josephson junction array, which is attached at the bottom. The microwave guide is isolated at the top (red spacer), to avoid external noise signals.

changing the output voltage from the Josephson voltage source: varying the frequency, changing the number of junctions in series or putting a tunable, low-noise voltage source in series to the Josephson voltage source. Each of the different options have their own pros and cons which will be elaborated next.

Tuning the voltage by varying the frequency

The least complicated way of changing the voltage $V_{1,N}$ is by changing the frequency f (see Eq. 3.2). The minimum step size adjustable with the microwave synthesizer is 4 kHz. For a Josephson voltage source with an output voltage of 1 V, this corresponds to a minimum step size of 60 nV. The scanning voltage range is limited by the microwave synthesizer due to

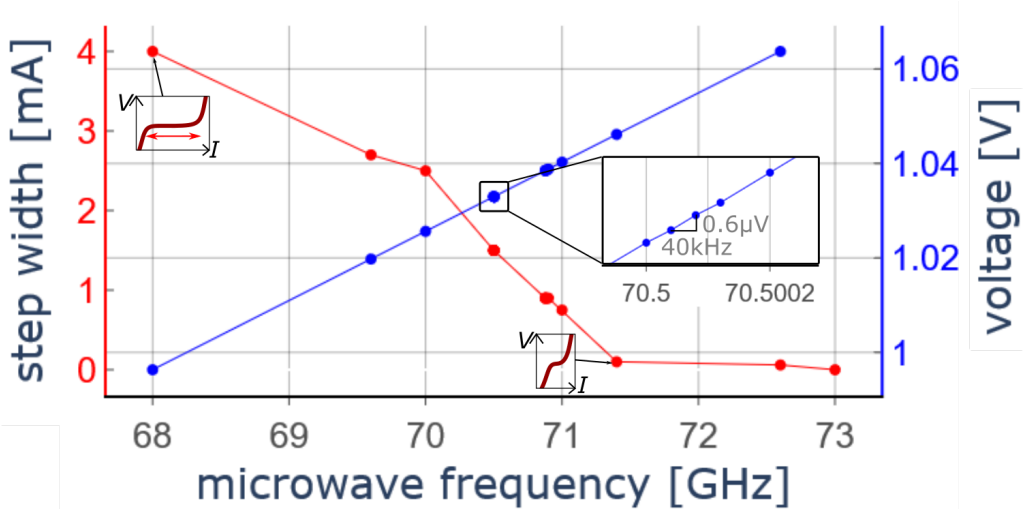

Figure 3.3: The Josephson voltage depends linearly on the microwave frequency (blue line), as predicted by Brian Josephson (Eq. (3.2), [Josephson, 1962]). The minimum step size of 4 kHz corresponds to 60 nV. With increasing frequency, the Shapiro step width (red line) decreases, until it vanishes (small insets). The microwave power was constant at 60 mW.

its operable range of 68.7 GHz to 72.9 GHz. These 4.2 GHz correspond to a change in output voltage of 60 mV for the 1 V junction. However, the microwave power depends strongly on the microwave frequency. This leads to a change in the Shapiro step width for different frequencies. For very narrow steps, the output voltage is not stable anymore. Experimentally, a maximum step size of 3.4 GHz corresponding to 50 mV was determined (compare Fig. 3.3). For smaller voltages, the tunability decreases linearly.

Drawbacks of this method are, besides the limited tunability, that the Shapiro step width not only decreases for certain microwave frequencies but also the center of the step wanders, such that the bias current has to be adapted for big changes (> 0.5 GHz) in frequency.

Tuning the voltage by varying the number of junctions in series

Another way of tuning the output voltage is by changing the number of junctions in series N (Eq. (3.2)). This can not be done arbitrarily. On the chip, there are prefabricated segments containing a certain number ($2^x, x \in [0; 12]$) of junctions. Voltages can be extracted from any segments in series, as illustrated in Figure 3.4. For other combinations (e.g. 4096+256 Josephson junctions), multiple bias sources would be needed.

The disadvantage of this method is, that before changing the segments, the bias current has to be set to zero to avoid flux. This could lead to the loss of a trapped particle.

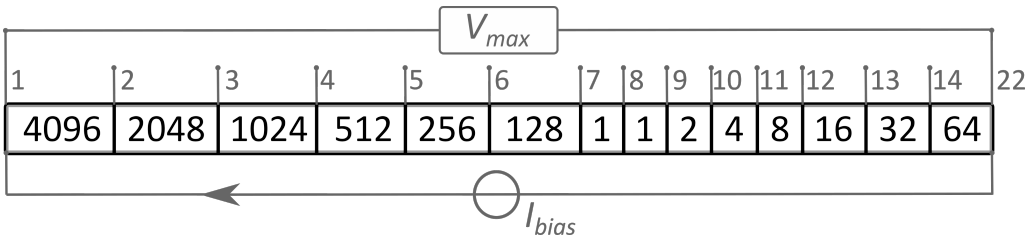

Figure 3.4: Physical order of segments vs. logical weight. The number of Josephson junctions per segment are potences of 2. The voltage can be extracted between any two taps (their numbering corresponds to the used Sub-D 25 connector attached to the dc pads on the Josephson voltage chip).

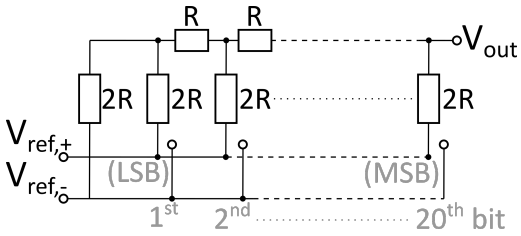

Figure 3.5: DAC working principle. The $R-2R$ ladder divides the reference voltage into the wanted output voltage. The least significant bit (LSB) stands for the smallest increment of the DAC output while the most significant bit (MSB) denotes the largest increment.

Tuning the voltage by adding a DAC in series to the junctions

An elegant way to circumvent the limited tunability of the above options is to put a tunable, low-noise voltage source in series to the Josephson voltage source ($V_{tot} = V_{JJ} + V_{DAC}$). A suitable device is the so-called voltage output **D**igital-to-**A**nalog **C**onverter (short: DAC). A DAC converts a series of digital signals with discrete time and amplitude value into an analog (continuous) output. The functionality is simple: a reference voltage V_{ref} is split by a ladder of resistors ($R-2R$ ladder) into the wanted output voltage. The resolution is determined by the number of bits, see Figure 3.5.

The stability of the output voltage V_{out} hence depends on the stability of the reference voltage V_{ref}, the thermal noise of the resistors R and noise contribution from the connectors and cables. In the scope of this thesis, two DACs were tested: the StaRep-DAC [Böhm et al., 2016], built in house and the industry manufactured DAC AD5791 [AD5791, 2022]. Both are low-noise, low-drift DACs and details about performance can be found in the provided data sheets.

The relative noise of a single DAC ($\Delta V'_{DAC}/V'_{DAC}$) compared to the relative noise of the compound of DAC and Josephson voltage source ($\Delta V_{tot}/V_{tot}$)

at equal absolute voltage $V'_{DAC} = V_{DAC} + V_{JJ}$ is calculated as follows:

$$\frac{\left(\frac{\Delta V'_{DAC}}{V'_{DAC}}\right)^2}{\left(\frac{\Delta V_{tot}}{V_{tot}}\right)^2} = \frac{\left(\frac{\Delta V'_{DAC}}{V'_{DAC}}\right)^2}{\frac{\Delta V^2_{DAC}+\Delta V^2_{JJ}}{(V_{DAC}+V_{JJ})^2}} = \frac{\Delta V'^2_{DAC}}{\Delta V^2_{DAC} + \Delta V^2_{JJ}} \approx \frac{\Delta V'^2_{DAC}}{\Delta V^2_{DAC}} \tag{3.3}$$

For this configuration there are three possible outcomes:

First, if the DAC noise increases with increasing DAC voltage, the absolute noise of the single DAC will be larger than the noise of the compound ($\Delta V'^2_{DAC} > \Delta V^2_{DAC}$). Hence, the larger the Josephson voltage, the smaller the noise of the compound will be. At the same time, a finite DAC voltage is required for tuning the output voltage. This case would be ideal for the experiment.

Secondly, the DAC noise can be independent of the absolute DAC voltage ($\Delta V'^2_{DAC} = \Delta V^2_{DAC}$). In this case, it makes no difference whether the DAC is used in conjunction with the Josephson voltage source or not.

At last, a small DAC output voltage means, that many resistor R are put into series to split the reference voltage. Each resistor contributes with thermal noise to the total DAC noise. Therefore, it may be that the DAC noise increases with decreasing DAC voltage. This means, the compound would perform worse than a single DAC ($\Delta V'^2_{DAC} < \Delta V^2_{DAC}$).

The possible outcome was experimentally tested and the results will be presented in the next section.

3.3 Voltage stability measurements

The voltage applied to the ring electrode of the analysis trap can be adjusted independently of the Josephson voltage source by connecting a low-noise, low-drift DAC in series with the junctions. It was investigated how well such a configuration performs in terms of noise. This section will present the measured stability of the two DACs (AD5791 and StaRep) at different output voltages, with and without the Josephson voltage source. To this end, the framework of voltage stability measurements is addressed first.

Voltage stability analysis

The standard deviation over N fractional voltage values y_i,

$$s = \sqrt{\frac{1}{N-1}\sum_{i=1}^{N}(y_i - \bar{y})^2}, \quad \text{with } \bar{y} = \frac{1}{N}\sum_{i=1}^{N} y_i, \tag{3.4}$$

should not be used for analyzing voltage stability. The problem is, that the standard deviation uses the deviation from the average $\bar{y}$, which changes for

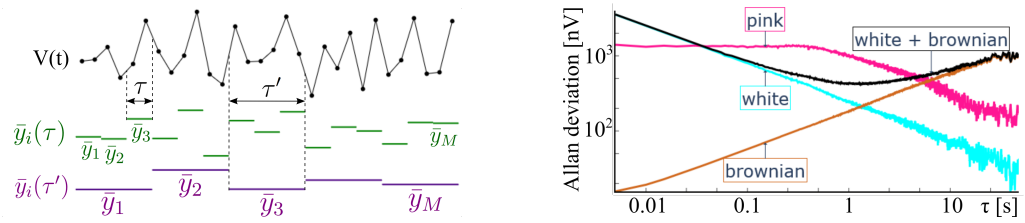

(a) (b)

Figure 3.6: Voltage stability analysis using Allan deviation plots. (a) A noisy voltage signal is averaged over different time intervals τ. These averages are used to calculate the Allan deviation (Eq. (3.5)), which is a measure for voltage stability. For more details, see text. (b) Allan deviation plot for different noise signals. A random signal with equal intensity at different frequencies is called *white noise*. For such a signal, the absolute noise is averaged out for larger τ. *Brownian noise* (or random walk) corresponds to drifts, occurring over longer time scales. Accordingly, the Allan deviation increases with large τ. Another example is *pink noise* (or 1/f noise), which has a power spectral density proportional to 1/f. It's noise contribution dominates on small averaging time scales.

drifting noise types [Riley and Howe, 2008]. This is resolved by using the Allan deviation $\sigma_y(\tau)$ instead, which represents a time-domain measure for the voltage stability. A small Allan deviation is a characteristic of a voltage source with high stability over the measured period. The Allan deviation is defined as

$$\sigma_y(\tau) = \sqrt{\frac{1}{2(M-1)} \sum_{i=1}^{M-1} \left(\bar{y}_{i+1} - \bar{y}_i\right)^2} \quad \text{[Allan and Barnes, 1981]}, \quad (3.5)$$

where $\bar{y}_i(\tau)$ is the i^{th} of M voltage values averaged over the measurement interval τ [Riley and Howe, 2008]. A noisy voltage signal over time and the respective averages over two different intervals τ and τ' are illustrated in Figure 3.6a. In the Allan deviation plot (Fig. 3.6b), the Allan deviation of a noisy signal is calculated for many different time intervals τ. In addition to the achieved voltage stability at a certain averaging time τ, the shape of the curve gives information about the different noise components (compare Fig. 3.6b). For example, a voltage signal consisting of white and Brownian noise will have an optimal averaging time τ at which the Allan deviation becomes minimal.

Performance of a Josephson voltage source in series to a DAC

The voltage stability of a Josephson junction has been measured to be better than three parts in 10^{19} [Jain et al., 1987, Tsai et al., 1983]. The voltmeters used in the following measurements (Keysight 3458A [Keysight, 2022] and Fluke 8508A [FLUKE, 2022]) cannot resolve such stable sources. Hence, by measuring the stability of the Josephson junction with these voltmeters, one receives the stability limit on the used voltmeters together with the connectors and cables. This was exploited to measure how the DAC noise scales with the absolute output voltage (Eq. (3.3)). Figure 3.7a illustrates the measurement setup: the StaRep DAC module is supplied with 10 V from the in-built precision reference voltage LTZ1000 [LTZ, 2022] whereas the AD5791 needs a 5 V supply which is provided from the external precision source UM1-14 [UM, 2022]. The output voltage of the DAC is measured differentially against the Josephson junction, set to the same output voltage as the DAC. Therefore, the voltmeter always measures in the zero volt range regardless of the output voltage of the DAC. Difficulties with the lower accuracy of the voltmeter at higher absolute voltages are eliminated in this way. As a general note concerning all measurements, the setup was situated in the non-temperature-stabilized cellar of the experimental hall (on the property of the Max-Planck Institute for Nuclear Physics) and connectors (preferably gold plated) were wrapped in tissues to avoid air currents influencing the voltage stability measurements. Non-shielded cable pairs were twisted for higher stability. The UM1-14 setup was wired with 4 mm (banana) connectors while the StaRep setup was wired with LEMO triax connectors. In the StaRep setup, the inner shield of the voltage reference has to be connected to the inner shield of the DAC output and both are put onto the external guard of the voltmeter, where the outer shield connects as well. The AD5791 DAC evaluation board makes this redundant. Here, only the output voltage low is connected to the voltmeter's external guard.

The AD5791 DAC output was measured against the Josephson voltage source for the three different output voltages 10 V, 5 V and 300 mV. The DAC has a buffered and non-buffered output. Both outputs were measured and do not show any significant difference ($< 1\sigma$) in noise behaviour. Hence, it will not be differentiated between the two outputs in the following. From Figure 3.7b it becomes evident, that the absolute noise decreases with the DAC output voltage. This means that a configuration of the DAC module in series to the Josephson voltage source, which allows tunability (see section 3.2), performs best for a small DAC output voltage. For a time of 100 s, which corresponds to the time required in the experiment to drive and detect a spin-flip, the measured DAC voltage stability is 121(16) nV, 64(9) nV and 41(6) nV at absolute voltages of 10 V, 5 V and 300 mV, with the respective reference voltage source. The noise originating from cables and connectors σ_{c+c} was measured separately and subtracted from the DAC measurements

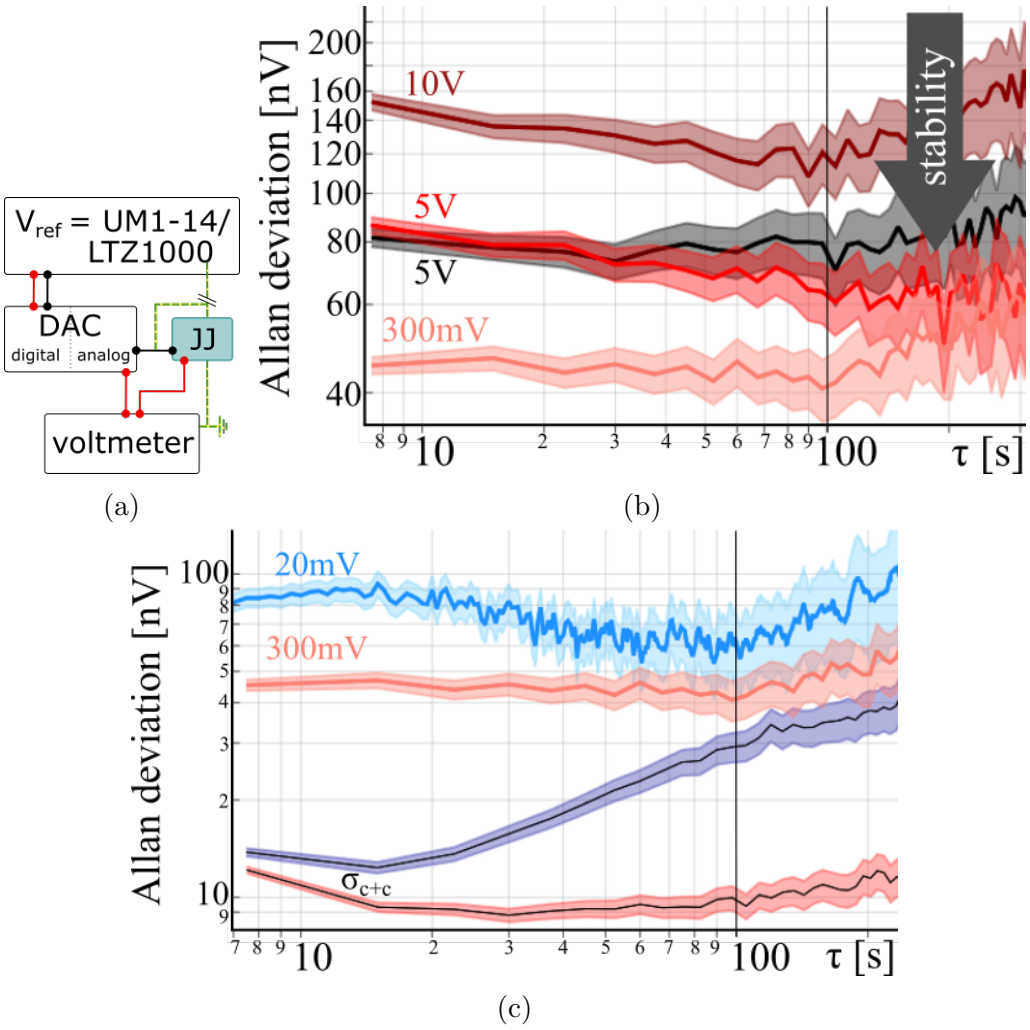

Figure 3.7: Noise behaviour of the AD5791 DAC (shades of red) and comparison to the StaRep DAC (shades of blue). (a) The AD5791 DAC is supplied with 5 V from the UM1-14 whereas the StaRep DAC is supplied with 10 V from the LTZ1000. Grounding (yellow-green dashes) occurs on the external guard of the voltmeter. For the StaRep setup, an additional grounding connection has to be established to the reference source (for details, see text). The DAC output voltage V_{DAC} = 10 V, 5 V, 0.3 V and 0.02 V is measured against the Josephson voltage source (JJ), such that the nanovoltmeter sees zero volt. (b) The AD5791 DAC voltage stability increases with decreasing output voltage (red curves). The UM1-14 at 5 V measured directly against the JJ (black curve) has a slightly higher Allan deviation than with the DAC in between. (c) The StaRep DAC (blue) at an output voltage of 20 mV is a bit less stable than the AD5791 DAC (salmon) at 300 mV. The noise contribution from cables and connectors (black line with red errors for the AD5791 and black line with blue errors for the StaRep) was subtracted from all measurements (Eq. (3.6)).

$$\sigma_{DAC+V_{ref}} = \sqrt{\sigma_{tot}^2 - \sigma_{c+c}^2} \tag{3.6}$$

yielding the displayed data. This reduces the total noise by 0.5 nV to 2 nV. The reference voltage was also directly measured against the Josephson voltage source at 5 V which is comparable to the DAC output at equal output voltage (black curve in Fig. 3.7b). Unexpected is the slightly larger noise contribution from the UM1-14 without a DAC module compared to the setup with DAC module in series, but the two measurements agree in the 1.3σ range.

A comparable measurement was carried out at the PTB with the StaRep DAC at an output voltage of 20 mV versus the Josephson voltage source. The data suggests that the StaRep DAC at 20 mV has a similar noise contribution as the AD5791 DAC at 300 mV - both agree in the 1.5σ range. However, taking into account that the StaRep DAC was measured at a fifteen times smaller output voltage, its voltage stability of 60(15) nV is expected to increase for larger voltages, whereas the AD5791 DAC at 300 mV is stable on the level of 41(6) nV. This suggests that the AD791 DAC is more stable for equal DAC voltages. All stabilities are given for a time interval of 100 s.

To exclude, that the difference in noise between the two DACs amounts from the different reference voltage sources, the two references were measured against the Josephson voltage source (see Figure 3.8). On the needed timescale of 100 s, the LTZ1000 supplying the StaRep DAC is with 52(10) nV slightly more stable than the UM1-14 with a voltage stability of 79(12) nV. Both values agree in the 1.5σ range. The measured stability is not limited by the resolution of the nanovoltmeter, as the green curve demonstrates where two arrays of the Josephson voltage source are measured against each other. This leads to the conclusion that the higher noise contribution of the StaRep DAC as compared to the AD5791 DAC does not originate from the reference voltages but from the DAC itself.

In a last measurement series, the performance of the two DACs was tested using the Josephson voltage source as reference voltage. Replacing the UM1-14 and the LTZ1000 with a Josephson voltage source should increase the absolute voltage stability, since the Josephson voltage source as reference is more stable than the other two reference sources (compare Figure 3.8). Since the Josephson voltage source was already used as reference and there is only one of its kind at the institute, these measurements are not differential against another Josephson voltage source in the voltmeter's zero volt range but absolute as the schematics in Fig. 3.9a show. Therefore, the lower resolution of the nanovoltmeter in the 0 V to 2 V range as compared to the

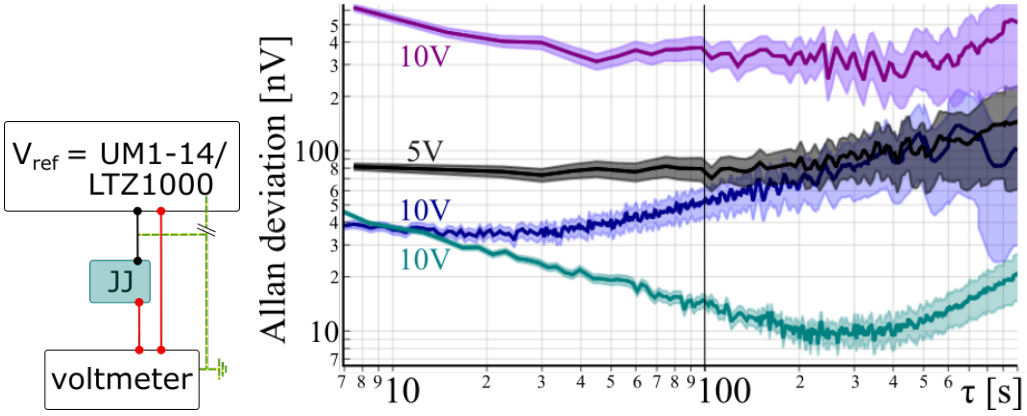

(a) (b)

Figure 3.8: Comparison of the performance of the reference voltage sources. (a) The reference sources UM1-14 and LTZ1000 are measured differentially against the Josephson voltage source (JJ) set to the same voltage, such that the nanovoltmeter measures at zero volt. (b) At 100 s, the UM1-14 with 5 V (black) has a slightly higher noise contribution than the LTZ1000 (blue) with 10 V. When replacing the reference voltage source with a Josephson voltage source (green), the stability limit of cables, connectors and the voltmeter are measured (18 nV at 100 s). The UM1-14 measured against the StaRep DAC with the LTZ1000 yields much higher voltage instability (purple).

0 mV to 200 mV range has to be kept in mind when looking at the data (Fig. 3.9b). Both DACs were measured at 1 V and 150 mV. The noise contribution from cables and connectors was subtracted.

In direct comparison, the StaRep DAC is less stable than the AD5791 DAC (see Fig. 3.9b), as was predicted in the previous measurement (Fig. 3.7b). With a voltage stability of 25(3) nV at 150 mV in the usual time interval of 100 s, the AD5791 DAC is much more suitable to be part of the ultra-stable tunable voltage source than the StaRep DAC with a stability of 155(11) nV. For the higher output voltage of 1 V, the voltage stability of both DACs decreases to 35(5) nV and 340(35) nV, for the AD5791 and the StaRep DAC, respectively. This is partly due to the higher measurement range of the nanovoltmeter, and partly because the DAC noise increases for higher output voltages (compare Fig. 3.7b).

The goal of these measurements is to determine whether the tested voltage source is sufficiently stable to achieve high spin-flip detection fidelity (see section 2.4) and at the same time tunable in the range of a few 100 mV - since the trap potentials must be matched to experimental reality (compare section 3.2). Therefore, a tunable, low-noise DAC can be put in series to

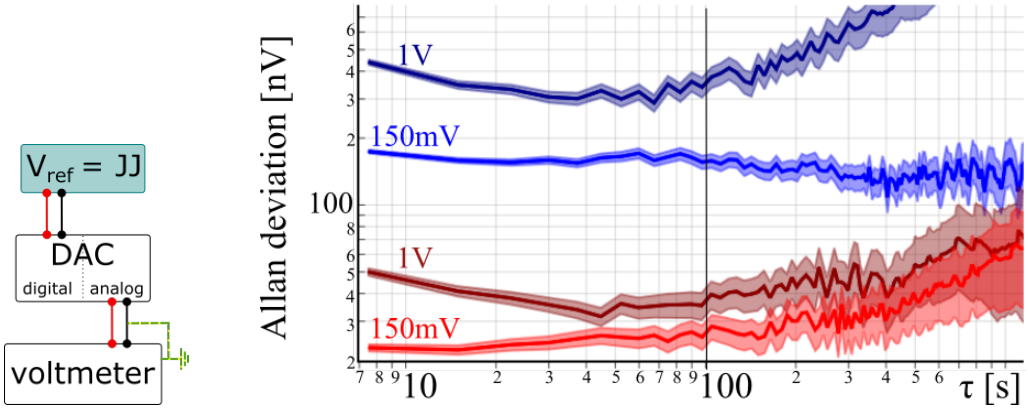

(a) (b)

Figure 3.9: Comparison of the performance of the StaRep DAC to the AD5791 DAC. (a) Using the Josephson voltage source (JJ) as reference, the voltage stability of the two DACs is measured directly on the nanovoltmeter for the two output voltages of 1 V and 150 mV. (b) The AD5791 DAC (red) has lower voltage fluctuations than the StaRep DAC (blue). The noise from cables and connectors was subtracted for both setups (see Eq. (3.6)).

the ultra-stable Josephson voltage source. With a stability of 25(3) nV over 100 s, the AD5791 DAC supplied by the Josephson voltage source enables a spin-flip detection fidelity of 98^{+1}_{-3}% while the trapping potential would be tunable in a range of ±150 mV. The tested StaRep DAC however is more noisy and would decrease the spin-flip detection fidelity to below 5 %. The DAC of choice is therefore the AD5791 DAC. Surprisingly, the UM1-14 performs at low output voltages of 0.5 V and below even better than the compound of Josephson voltage source and AD5791 DAC with a stability of 22(3) nV over 100 s (compare Fig. 3.10). Hence for small voltages, this source is not only user friendly but also extremely stable, enabling a spin-flip detection fidelity of $99.2^{+0.4}_{-2.7}$%.

The correction electrodes have a smaller influence on the trapped particle and therefore, their required voltage stability is of the order of 50 nV. An UM1-14 which is temperature stabilized to 25 °C exceeds this stability criterion with fluctuations in the 40 nV range over 100 s averaging time at 2 V output voltage [Bock, 2022] (see Fig. 3.10). Hence, no combination of Josephson voltage source and DAC is needed but the UM1-14 supplying the correction electrodes is sufficient. The results are discussed in chapter 5.

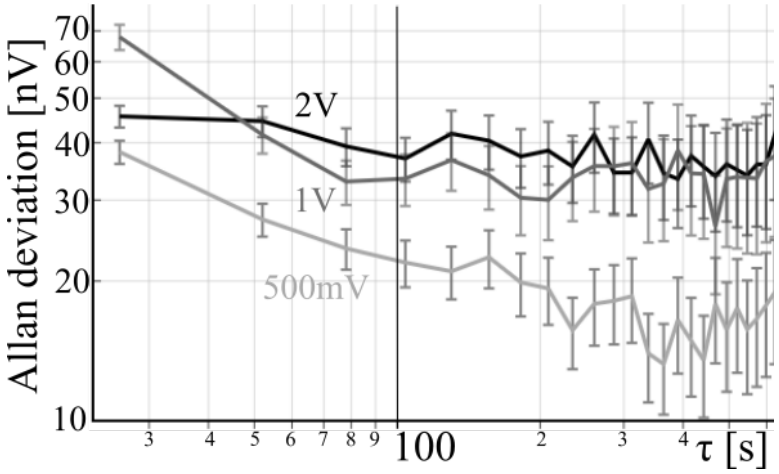

Figure 3.10: Voltage stability of the UM1-14 for low output voltages. The UM1-14 was temperature stabilized to 25 °C and directly measured on the nanovoltmeter for output voltages of 500 mV, 1 V and 2 V.

4 Implementation of a laser cooling scheme for $^3He^{2+}$

Laser cooling of trapped beryllium $^9Be^+$ ions plays an important role in many physics experiments dealing with e.g. quantum information processing [Home et al., 2009], quantum-logic optical clocks [Chou et al., 2010] and quantum-logic spectroscopy [Schmidt et al., 2005]. In Penning-trap experiments, it can be used to sympathetically laser-cool ions with no suitable laser-cooling transition such as the proton, antiproton [Bohman et al., 2018], highly charged ions [Tu et al., 2021] or in this case the helion. Doing so, temperatures in the low mK range can be reached in the ion's axial mode, facilitating the spin-flip detection.

In the sympathetic laser-cooling scheme, the axial motion of a cloud of $^9Be^+$ ions confined in a Penning trap is laser cooled to the Doppler limit. With the mean lifetime of the $^9Be^+$ excited state being $\tau = 8.1(4)\,\mathrm{ns}$ [Andersen et al., 1969], the Doppler cooling limit is given by

$$T_D = \frac{\hbar}{2k_B\tau} = 0.47(2)\,\mathrm{mK}. \tag{4.1}$$

By coupling the axial motion of $^3He^{2+}$ and the $^9Be^+$ cloud, the helion can be sympathetically cooled. The helion's axial temperature T_{He} will depend on the coupling strength between helion and beryllium ions and the coupling to heating sources, such as electronic noise and detector couplings. By applying an rf pulse, which couples the axial and cyclotron mode, the cyclotron energy E_+ can be reduced to $E_+ = E_z \cdot \omega_+/\omega_z$ [Bohman et al., 2018]. Inserting the eigenfrequencies $\nu_+ = 58.2\,\mathrm{MHz}$ and $\nu_z = 370\,\mathrm{kHz}$ (Eq. (2.4)) of helion in the precision trap, a minimal cyclotron temperature of

$$T_+ = T_D \cdot \nu_+/\nu_z = 74\,\mathrm{mK} \tag{4.2}$$

can be reached. Laser cooling of $^9Be^+$ typically requires a single laser beam, which is slightly red detuned from the cycling transition between ground state $^2S_{1/2}$ and excited state $^2P_{3/2}$. This transition with a wavelength of roughly 313 nm ($\widehat{=}$ 957 THz) becomes shifted due to the Zeeman effect in the presence of the Penning trap's magnetic field. The first section hence deals with determining the precise laser-cooling transition frequency in the B-field of the experiment.

The beryllium used for laser cooling is produced on top of the trap tower with the help of a second laser. A pulsed, frequency-doubled high-energy

Nd:YAG laser [Litron, 2022] ablates beryllium from a solid metallic CuBe target, provided that the laser beam is well aligned and focused. The alignment scheme for the cooling and ablating laser beams is presented in section 4.2.

Section 4.3 describes the experimental implementation of the cooling laser while the theoretical model of laser, detector and ion interaction is treated in section 4.4. At last, a measurement demonstrating laser cooling is presented in section 4.5, from which the laser cooling rate and the temperature of the beryllium ions can be extracted.

4.1 $^9Be^+$ laser cooling transitions

The level structure of $^9Be^+$ features a fine and hyperfine structure, which is split into additional levels in a magnetic field (compare Fig. 4.1). For strong magnetic fields ($\mu_{J,I}B > \mu_N$), like the one used in the experiment, this splitting can be described by the Paschen-Back effect [Paschen and Back, 1912] which is the strong-field limit of the Zeeman effect. Here, the coupling between nuclear spin $\bar{I}$ and total electronic angular momentum $\bar{J}$ is disrupted and the states are no longer degenerate.

The Hamiltonian of such a system is composed of the field-free Hamilton operator and the interactions of the magnetic moment of total electronic angular momentum and nuclear spin [Hertel and Schulz, 2015]:

$$\hat{H}_{HFS} = \frac{A}{\hbar^2}\hat{\boldsymbol{I}}\hat{\boldsymbol{J}} + \frac{B}{\hbar}\left(g_J\mu_B\hat{J}_z - g_I\mu_N\hat{I}_z\right), \tag{4.3}$$

with the Bohr μ_B and nuclear μ_N magneton, the nuclear g-factor g_I, and the reduced Planck constant $\hbar$. The hyperfine structure constant A parameterizes the splitting of energy levels at zero magnetic field, caused by the interactions between the electronic and the nuclear electromagnetic moment. The Landé g-factor is defined as

$$g_J = g_L\frac{J(J+1) - S(S+1) + L(L+1)}{2J(J+1)} - g_S\frac{J(J+1) + S(S+1) - L(L+1)}{2J(J+1)}. \tag{4.4}$$

The appropriate basis in the Paschen-Back regime is $|Jm_JIm_I\rangle$. Using the relations

$$\begin{aligned}
&\hat{\boldsymbol{I}}\hat{\boldsymbol{J}} = \hat{I}_z\hat{J}_z + \frac{1}{2}\left(\hat{I}_+\hat{J}_- + \hat{I}_-\hat{J}_+\right),\\
&\hat{I}_z\,|Jm_JIm_I\rangle = \hbar m_I\,|Jm_JIm_I\rangle\,, \quad \hat{J}_z\,|Jm_JIm_I\rangle = \hbar m_J\,|Jm_JIm_I\rangle \quad \text{and}\\
&\hat{I}_\pm\,|Im_I\rangle = \hbar\sqrt{I(I+1) - m_I(m_I \pm 1)}\,|Im_I \pm 1\rangle \quad \text{(analogous for } \hat{J}_\pm\text{)},
\end{aligned} \tag{4.5}$$

with the ladder operators $\hat{I}_\pm$ and $\hat{J}_\pm$, the Hamiltonian can be evaluated. In matrix notation, this yields

$$\begin{aligned}
&\langle Jm_{J'}Im_{I'}|\,\hat{H}_{HFS}\,|Jm_JIm_I\rangle = \\
&(Am_Im_J + (g_J\mu_B m_J - g_I\mu_N m_I))\,\delta_{m_{J'},m_J}\delta_{m_{I'},m_I} \\
&+\frac{A}{2}\sqrt{J(J+1)-m_J(m_J-1)}\sqrt{I(I+1)-m_I(m_I+1)}\delta_{m_{J'}m_{J-1}}\delta_{m_{I'}m_{I+1}} \\
&+\frac{A}{2}\sqrt{J(J+1)-m_J(m_J+1)}\sqrt{I(I+1)-m_I(m_I-1)}\delta_{m_{J'}m_{J+1}}\delta_{m_{I'}m_{I-1}}.
\end{aligned} \tag{4.6}$$

The energy level shift in a magnetic field B is calculated by solving the eigenvalue problem of this matrix. For beryllium with nuclear spin $I = 3/2$, these shifts have been calculated in the magnetic field $B_{CT} = 5.7206\,\mathrm{T}$ present in the coupling trap. The B-field value has been experimentally determined by S. Dickopf via ν_c measurements. An overview of all energy level shifts can be found in the appendix Table B.2.

The two suitable cycling transitions $\nu_{L,\pm}$ for laser cooling $^9\mathrm{Be}^+$ are between the ground and excited state manifolds:

$$^2S_{1/2}\,|m_J = \pm 1/2, m_I = \pm 3/2\rangle \quad \leftrightarrow \quad ^2P_{3/2}\,|m_J = \pm 3/2, m_I = \pm 3/2\rangle\,,$$

as illustrated in Fig. 4.1.

In the Penning trap, the $^9\mathrm{Be}^+$ ions are Doppler cooled in one dimension by using a single laser beam, which is slightly red detuned from $\nu_{L,\pm}$. For beryllium ions moving towards the laser beam, its frequency is Doppler shifted towards the transition frequency and the probability for stimulated absorption increases. The electron will subsequently decay from the excited state $2p^2P_{3/2}$ to the ground state $2p^2S_{1/2}$ by emitting a photon into a random direction. After many cycles of stimulated absorption and spontaneous emission, the photon emission recoil averages out and the only force acting on the beryllium ion is that along the laser beam. In the case the electron decays into the dark state $^2S_{1/2}\,|m_J = -1/2\rangle$ or $^2S_{1/2}\,|m_J = +1/2\rangle$ for the $\nu_{L,\pm}$ transitions, respectively, repumping occurs for light with circular polarization $\sigma^\pm$ along the quantization axis. All used values are summarized in Table 4.1 along with the resulting transition frequencies.

4.2 Laser alignment

The experiment makes use of two different laser beams: In addition to the UV-laser used for laser cooling $^9\mathrm{Be}^+$ at a wavelength of roughly 313 nm, a pulsed frequency-doubled Nd:YAG laser with a wavelength of 532 nm is installed for ablating beryllium from a solid CuBe target. Both beams, the UV and the Nd:YAG, enter the experiment from the top and travel parallel

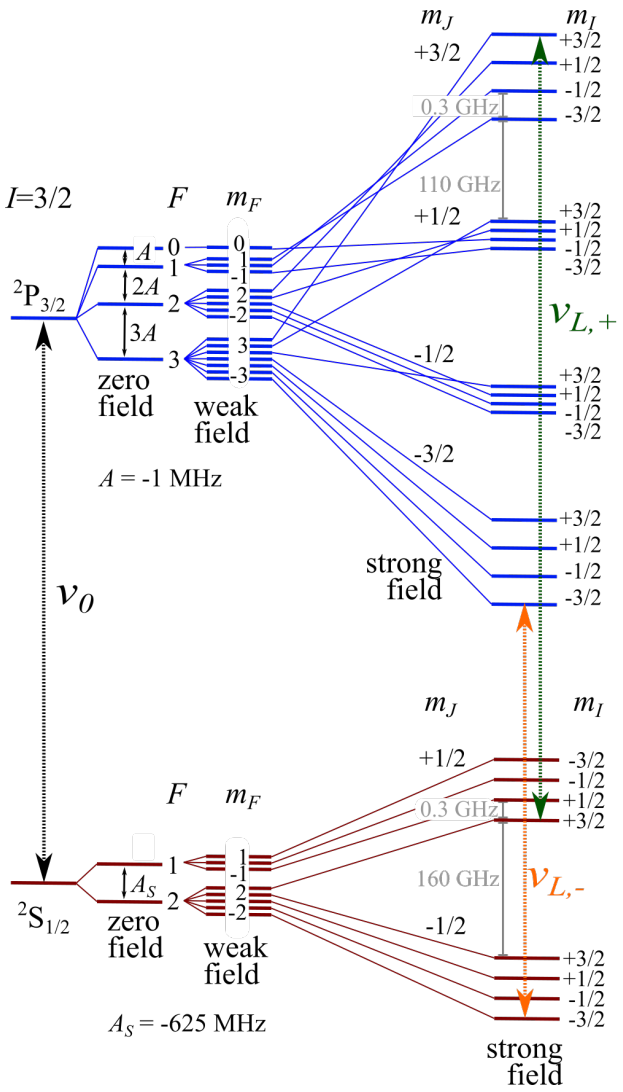

Figure 4.1: Beryllium energy level splitting in presence of a weak and strong magnetic field. The laser cooling transitions in the strong-field regime are found between the $^2S_{1/2}\,|m_J = \pm 1/2, m_I = \pm 3/2\rangle$ and $^2P_{3/2}\,|m_J = \pm 3/2, m_I = \pm 3/2\rangle$ states (green and orange dashed arrows). The zero field transition frequency ν_0 is illustrated as black dashed arrow. The $^2P_{1/2}$ state, located between the $^2S_{1/2}$ and $^2P_{3/2}$ state, is not shown.

	hyperfine structure constants A	
A_S	$-625.008\,837\,048(10)_{exp}$ MHz	[Wineland et al., 1983]
$A_{P,3/2}$	-1.018(3)$_{theo}$ MHz	[Puchalski and Pachucki, 2009]
	g-factors	
g_L	1	
g_I	-0.7848654635	[Wineland et al., 1983]
g_S	-2.0023193044	[CODATA, 2022]
	laser cooling frequencies	
$\nu_0(0\,\mathrm{T})$	957.396 80(13) THz	[Bollinger et al., 1985]
$\nu_{L,+}(B_{CT})$	957.477 34(13) THz	Eq. (4.6)
$\nu_{L,-}(B_{CT})$	957.317 20(13) THz	Eq. (4.6)
$\nu_{L,+}(B_{CT})/2$	478.7386(7) THz	Eq. (4.6)
$\nu_{L,-}(B_{CT})/2$	478.6586(7) THz	Eq. (4.6)

Table 4.1: $^9Be^+$ laser cooling transitions calculated with Eq. (4.6) at a magnetic field strength of $B_{CT} = 5.7206\,\mathrm{T}$. The zero field transition frequency ν_0 between the $2p\ ^2S_{1/2} \leftrightarrow 2p\ ^2P_{3/2}$ states is split into a manifold by the strong magnetic field. Laser cooling within a closed cycle works for the $^2S_{1/2}\,|m_J = \pm 1/2, m_I = \pm 3/2\rangle$ to $^2P_{3/2}\,|m_J = \pm 3/2, m_I = \pm 3/2\rangle$ transitions, with frequency $\nu_{L,\pm}$. The errors are dominated by the error on ν_0, the B-field error is below 0.2 mT. The frequency $\nu_{L,\pm}/2$ is used for controlling the laser frequency and stability, as discussed in section 4.3.

to each other to a photon detector below the trap chamber and the beryllium target, respectively. Mirrors and photon detectors are put in various places along the laser beam path to enable the alignment. A schematic layout of the beam paths on the laser table and through the experiment is illustrated in Figure 4.2 and Figure 4.3, respectively.

The laser alignment is divided into three steps: Within the experiment, only the UV laser beam path can be detected. Therefore, in a first step, the lasers must be aligned parallel. Then, using the same mirrors for both beams, the UV laser is guided through the trap chamber with the help of a beamsplitter, fluorescence plates and photon detectors. Simultaneously, the Nd:YAG laser enters the experiment through a pipe in parallel to the UV laser. At last, the fine adjustment requires optimizing the laser beam signal on the photon detectors. In case of the ablation laser, the signal of the FFT resonator spectrum is optimized simultaneously. More details on each step will be given next.

Parallelization of two laser beams

To align a single laser beam in space, two mirrors are sufficient. Therefore, four mirrors are needed for aligning two beams. The beams are brought

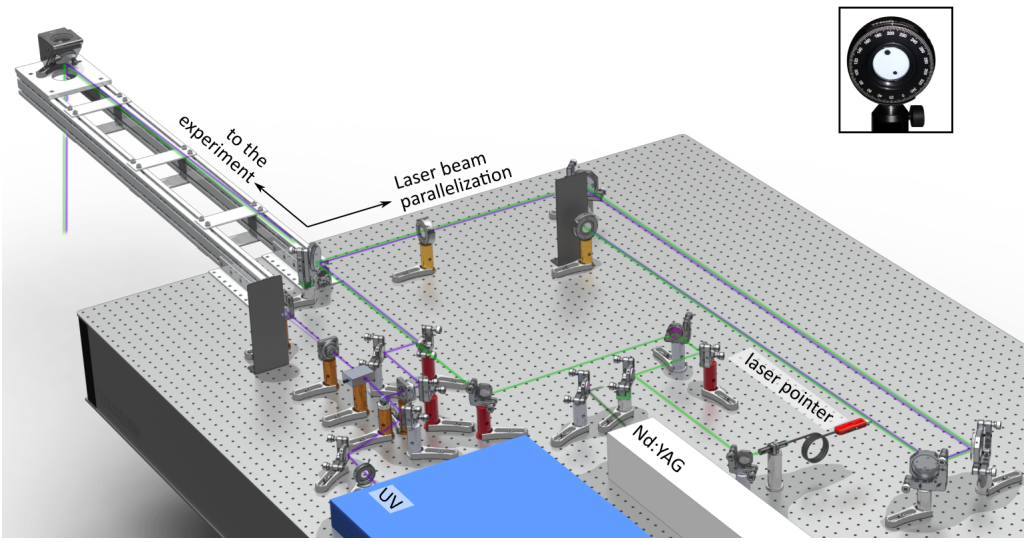

Figure 4.2: For laser alignment, the UV laser beam (purple) and the Nd:YAG laser beam (dark green) are parallelized. A mirror on a flip mount is used to superimpose a green laser pointer (bright green), used for the alignment process, to the Nd:YAG laser beam. The mirrors placed on red posts are used for the alignment in space. On top of the golden posts, the adjustment plates are mounted (enlarged in the inset). For more details, see text. The brown posts belong to the *acousto-optic modulation* (AOM) setup, which will be discussed in section 4.3.

next to each other with either a *dichroic mirror*, which in our case reflects light in the UV regime while longer wavelengths such as the Nd:YAG laser are transmitted, or a *D-shaped mirror*, which is put into the path of one beam without cutting off the second beam. The second method is now used in the experiment, as the power loss of the beams is smaller after a D-shaped mirror.

The continuous wave UV laser is made visible by placing paper into the beam path. White paper contains optical brightening agents, which are chemical compounds that absorb light in the UV region of the electromagnetic spectrum, and re-emit light in the blue region by fluorescence. With the pulsed Nd:YAG laser, adjusting the beam is more difficult, even at a high pulse frequency. Instead, a green laser pointer that is superimposed to the Nd:YAG laser beam path with the help of a flip mounted mirror is used for the complete alignment process (compare Fig. 4.2).

In the experiment, the centers of the UV and Nd:YAG laser beams are a distance of 1.5 cm apart, and their targets are approximately 3.5 m away from the four parallelization mirrors. To ensure, that both beams hit their targets, the two beams have to be parallelized along a distance greater than

4 m.

There is an adjustment plate at the beginning and end of this parallelization path, with holes indicating where the beams have to go through (see inset of Fig. 4.2). A limit on the parallelization is given by the accuracy with which the beam center passes through the hole center. With these plates, the distance between the two beams becomes fixed.

Another degree of freedom is the position of one beam relative to the other in relation to the laboratory frame. When the UV laser is fixed, there is an entire circle on which the Nd:YAG laser is at the correct distance from the UV laser. This is accounted for by mounting the adjustment plates on an indexed rotary mount (inset of Fig. 4.2). The correct rotation is adjusted optically on the location where the beams enter the experiment. A fluorescent plate surrounds the pipe for the Nd:YAG laser, showing whether parts of the beam are cut off from the pipe. This way, both beams enter their respective pipe but they still have to be adjusted in order to reach the trap chamber and the beryllium target in a distance of 1.8 m.

Rough adjustment

At this stage, the UV laser beam and the Nd:YAG laser beam are parallel with proper orientation in the laboratory frame, and both beams enter the experiment through their intended pipes. However, they are not aligned with the pipes yet and therefore may not go through all the way to their respective targets. Only in the UV laser beam path, there are detection and alignment tools installed. Hence, the Nd:YAG laser (and the green laser pointer used for alignment) can be turned off for the rough adjustment and will not be discussed in the following. The Nd:YAG beam is aligned simultaneously with the UV laser beam as they are parallel and share the same mirrors.

On top of the experiment, a 27 cm x 30 cm breadboard holds four more mirrors: the first is a 90° mirror used for reflecting the beams coming from the laser table into the plane of the breadboard. Then, two adjustment mirrors are used for aligning the beams parallel to the pipes. At last, another 90° mirror guides the beams from the breadboard plane through the experiment (see Fig. 4.3b).

The UV laser enters the experiment through a glass flange, behind which the pipes in the pre-vacuum chamber are situated. The beam-splitter located 15 cm below the glass reflects a small fraction of the beam in a 90° angle, while the main beam is transmitted. This reflection passes through two fluorescent plates (12 cm apart) with a hole marking the center (Fig. 4.3c) and then hits a 4-quadrant diode. Once the reflected beam passes through the center of the fluorescent plates and hits the center of the 4-quadrant diode, the main beam goes through the pipe to the trap chamber. In the current setup, the cage system with fluorescent plates and 4-quadrant

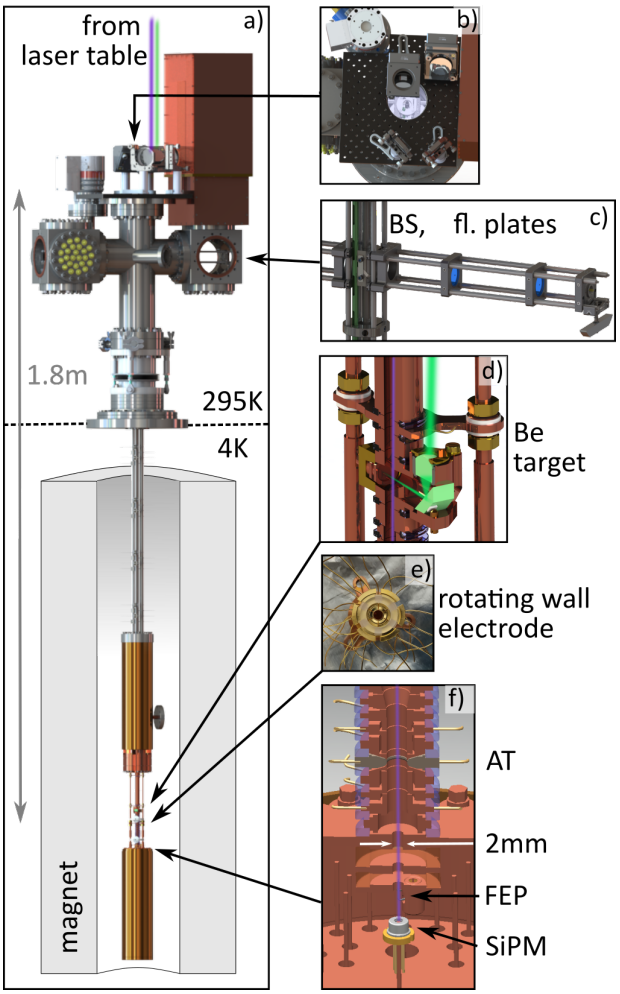

Figure 4.3: The two laser beams enter the experimental setup (a) from the top via four guiding mirrors (b). The UV laser beam is aligned vertically by adjusting a 90° reflection from the beamsplitter (BS) with the help of fluorescent plates (c). The Nd:YAG laser beam is focused onto a solid beryllium target with a lens and a mirror (d) directly above the trap tower. SiPMs around the split electrode enable the detection of stray light and fluorescent light (e). Below the trap tower and the field emission point (FEP), another SiPM is situated, that detects the UV beam through a 2 mm hole in the FEP electrode (f). The figures are the modified CAD models of B. Moerk, except for the photograph in (e).

diode unfortunately slipped down due to its weight by approximately 1 mm such that the beam no longer goes through the center of the plates but slightly above the center hole. In addition, the beam no longer reaches the diode. This makes the alignment less precise. Regardless, an additional fine adjustment step is necessary, in which the beam path is optimized using photon detectors in the trap tower region.

Fine adjustment

In the fine adjustment process, the UV laser path and the Nd:YAG laser path are optimized separately. The UV laser fine adjustment is treated first.

The ring electrode on the beryllium cooling trap is divided into six parts (Fig. 4.3e). Different potentials (even periodically changing potentials) can be applied to each part, therefore this electrode is called *rotating wall electrode*. Behind each slit, a silicon photomultiplier (SiPM) is situated, detecting stray light from the UV beam even at cryogenic temperatures [Biroth et al., 2016, SiPM, 2022]. Beneath the trap chamber, another SiPM is placed (Fig. 4.3f). If the UV beam passes the trap chamber without scattering on the walls, the signal on the detector below the trap chamber should be maximal whereas the signal on the detectors behind the rotating wall electrode should be minimal. Exemplary signals on the detectors after fine adjusting the UV laser beam are:

0.7 mV :	SiPM below the trap chamber
2000 counts/0.5 s :	three SiPMs behind the rotating wall electrode
160 µW :	UV beam power before the breadboard mirrors.

Stray light from the green laser pointer used for aligning the Nd:YAG laser beam can be seen on the detectors behind the rotating wall electrode. The beam path is optimized by maximizing this signal. In addition, beryllium was only loaded, when the FFT offset of the resonator from the cooling trap increased. Successful loading parameters are:

560 000(2500) counts/0.5 s :	three SiPMs behind the rotating wall electrode
8(1) dB :	increase of FFT resonator offset
5 mJ ($\widehat{=}$ 32 att. setting) :	attenuation of the Nd:YAG laser.

After ablating beryllium from the target, many ($\simeq$ 1000) beryllium ions are captured in the cooling trap. However, at very high ion numbers, the ions do not thermalize with the resonator. A dip could be produced only for roughly 30 to 40 ions.

4.3 UV-laser frequency modulation and control

For efficient laser cooling, the frequency of the UV-laser has to be red detuned from the transition frequency calculated in section 4.1. The short lifetime τ of the electrons in the excited state $2p^2P_{3/2}$ is associated with the natural linewidth $\Gamma = 1/(2\pi\tau) = 19.6(10)\,\mathrm{MHz}$ of this transition. Modulating the laser frequency around this transition and observing the fluorescent light from the spontaneous emission is useful for e.g. measuring the temperature of the beryllium ions. Therefore, the first part will deal with setting the laser beam frequency, whereas the second part treats the modulation of the laser beam frequency.

The UV-laser is a frequency-quadrupled high-power diode laser [TOPTICA, 2022] with the second harmonic generation in the near-infrared and the fourth harmonic generation in the ultra-violet at approximately 313 nm. Coarse tuning is achieved with an adjustment screw on the laser, which shifts the angle of the diode laser grating. For fine tuning, the piezo control current is changed using a proportional integral (PI) controller.

The frequency of the UV-laser is measured with a wavelength meter [HighFinesse, 2022], which compares the second harmonic generation with an iodine stabilized helium-neon laser [Lasertex, 2022]. The helium-neon laser has a high frequency stability below 2.5×10^{-12} (10 s averaging time) and the absolute frequency of the respective mode is well known to 6×10^{-12}. Therefore, it represents an ideal frequency laser standard.

When the laser frequency is tuned to maximum cooling, the signal on the SiPMs surrounding the rotating wall electrode should increase due to the photons emitted from spontaneous emission. These photons make up the *fluorescent light* and must be detected against the background of *stray light*. Initially, the beryllium ions at the resonators temperature of roughly 10 K are Doppler broadened in the range of a few hundred MHz, which is much larger than the natural linewidth Γ =19.6(10) MHz of the laser cooling transition. Therefore, the fluorescent photon rate is expected to be much smaller than the background of stray light. In this case, no difference is observed in the photon signal for efficient and non-efficient laser cooling. Various methods have been developed to increase detection sensitivity. One of them involves modulating the laser with an acousto-optic modulator (short: AOM) and feeding the photon signal into a lock-in amplifier which extracts very small signals buried in noise. The advantage of using an AOM instead of modulating the laser frequency with the PI controller is, that much higher modulation frequencies can be reached.

Within an AOM, a standing sound wave diffracts the incident light into several orders for the Bragg condition:

$$\theta_B \simeq sin(\theta_B) = \frac{m\lambda}{2n\Lambda}, \tag{4.7}$$

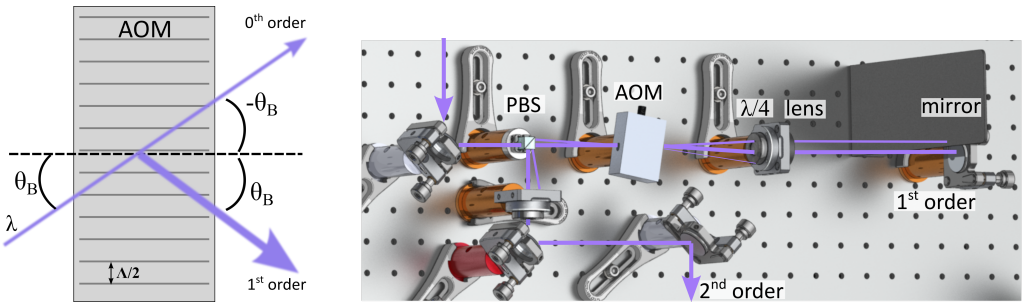

(a) (b)

Figure 4.4: Acousto-optic modulator (AOM). a) Incident light at the Bragg angle θ_B is partly transmitted and partly diffracted in an AOM. The AOM can be tilted such that most laser beam power is diffracted into the first order. Higher orders will be weaker but still present. The angle is largely exaggerated. b) AOM setup in the experiment. The UV laser is transmitted through a polarizing beamsplitter (PBS), passes the AOM, a $\lambda/4$ plate which rotates the polarization and a lens parallelizing the diffracted beams. The mirror reflects the 1st order back through the AOM and the PBS reflects the beam with rotated polarization. When modulating the laser frequency, the 2^{nd} order stays fixed in space.

where λ and θ_B are the wavelength and the Bragg angle of the incident beam, n is the refractive index within the AOM and Λ is the wavelength of the standing sound wave (compare Fig. 4.4a). In the Bragg regime, the first order diffraction $m = +1$ is most efficient, while there is hardly any loss into other orders.

The frequency of the outgoing laser now depends on the frequency of the standing wave c/Λ, which can be modulated with a few MHz. However, the angle of the outgoing beam also changes with Λ. An easy way to modulate the laser frequency and at the same time leave the laser beam alignment fixed, is by double passing the AOM. After the first pass, the angle of the first order is θ_B. The second pass through the AOM diffracts the beam by $-\theta_B$, cancelling the shifts altogether. By introducing a $\lambda/4$-plate which the beam double-passes, the polarization is rotated by 180° such that the incoming and outgoing beam can be separated with a polarizing beamsplitter. The setup is illustrated in Figure 4.4b. The diffraction of the laser beam into different orders is pictured in Figure 4.5a.

The detection sensitivity to fluorescent light is increased by placing a lock-in amplifier behind the photon signal. Far from resonance, no laser cooling occurs and the photon signal is constant. Near resonance, the number of

laser cooled ions changes with the modulation frequency and with that the number of fluorescent photons. If the laser frequency $\omega_L = \omega_0 + \Delta\omega \sin(\Omega t)$ is changed periodically with the modulation frequency Ω and a hub of $\Delta\omega$, the transmitted laser power P_t can be developed into a Taylor series around the center frequency ω_0:

$$P_t(\omega_L) = P_t(\omega_0) + \sum_n \frac{\Delta\omega^n}{n!} \left(\frac{d^n P_t}{d\omega^n} \right) \Bigg|_{\omega_0} \sin^n(\Omega t). \tag{4.8}$$

Given that the fluorescence signal $f(\omega)L \ll 1$ is small, with the fluorescent coefficient $f(\omega)$ and the length along which photon absorption occurs L, the transmitted power P_t is in first order equal to

$$P_t(\omega) = P_0 \exp\left(-f(\omega)L\right) \simeq P_0 \left[1 - f(\omega)L\right]. \tag{4.9}$$

If the laser power P_0 is independent of the frequency ω, Equation (4.8) can be rewritten with

$$\left(\frac{d^n P_t}{d\omega^n} \right) \Bigg|_{\omega_0} = -P_o L \left(\frac{d^n f(\omega)}{d\omega^n} \right) \Bigg|_{\omega_0}. \tag{4.10}$$

With trigonometric functions, the $\sin^n(\Omega t)$ powers can be converted into functions of $\sin(n\Omega t)$ and $\cos(n\Omega t)$. For a sufficiently small modulation hub $\Delta\omega/\omega_0 \ll 1$ the higher powers of $\Delta\omega^n$ can be neglected, and the signal normalized to the input power at frequency $n\Omega$ is given by

$$\begin{aligned} S(n\Omega) &= \frac{P_t(\omega) - P_t(\omega_0)}{P_0} \\ &\propto \Delta\omega \frac{df}{d\omega} \sin(\Omega t) + \frac{\Delta\omega^2}{4} \frac{d^2 f}{d\omega^2} [1 - \cos(2\Omega t)] - \frac{\Delta\omega^3}{24} \frac{d^3 f}{d\omega^3} \sin(3\Omega t). \end{aligned} \tag{4.11}$$

By setting the phase-sensitive lock-in amplifier [ZurichInstruments, 2022] to the harmonic $n\Omega$ of the modulation frequency Ω, essentially the $n-$th derivative of the fluorescence coefficient $f(\omega)$ is measured. The higher orders $d^n f/d\omega^n$ are large for the fluorescent signal and small for the background. This way, even small transitions in presence of a broad spectral background can be detected [Demtröder, 2013].

The AOM [AOM, 2022] was implemented into the laser beam path. After passing through the AOM, the laser beam power of the second order is decreased by 30 % to 50 % with respect to the non-modulated beam. The laser beam alignment is independent of the modulation as predicted. However, it turned out that the laser beam power coming out of the AOM P_0 strongly depends on the modulation hub: A hub of $\Delta\omega = 10\,\mathrm{MHz}$ at an operating

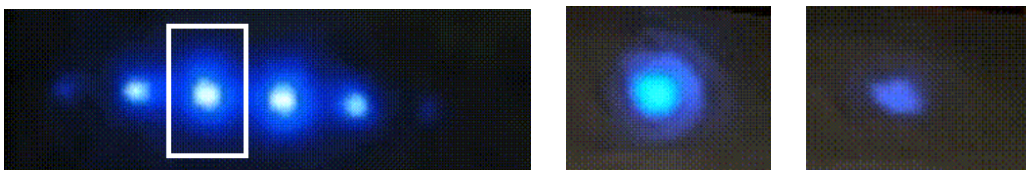

(a) (b) (c)

Figure 4.5: A laser beam passing through an AOM becomes diffracted into multiple orders of different frequency. (a) The orders are spatially separated. The angle of incident beam can be adjusted such that most laser power is diffracted into the second order after the double pass (dot within box). (b),(c) For large modulation hubs, the efficiency with which light is diffracted into the second order varies.

frequency of $\Omega = 100\,\mathrm{MHz}$ changes the output power by 35 % (see Figure 4.5b and 4.5c), but also for smaller frequency hubs a power dependence is observed. Instead of solely modulating the frequency of the laser beam, it's amplitude is simultaneously modulated. The lock-in amplifier therefore picks up the modulated background signal, and the fluorescent light is buried in noise after all.

This problem might be circumvented by using the amplitude modulated beam as a reference signal for the lock-in amplifier and using this signal as an offset on the photon detector. In addition, the new setup features apertures in front of the SiPMs to reduce the amount of stray light reaching the detectors since a general problem was the shift in electrode voltages once the laser was in operation.

4.4 Laser-ion interaction

Trapped ions induce image charges in the outer electrodes which are detected by a resonator circuit, as described in section 2.2. When the ions' axial energy is in thermal equilibrium with the detection system, a noise dip appears in the FFT spectrum. Once the ions are laser cooled, their axial energy is reduced below the equilibrium temperature of the detection system. As a result, the noise dip disappears. With a blue detuned laser, the ions' axial energy is increased above the detector energy, which leads to a peak signal in the FFT spectrum [Sturm, 2011]. The line shape of such a dip signal reflects the coupling strength of the ions to the laser and the detection system. The theoretical model of this line shape and what can be extracted from it is treated in this section.

The equivalent circuit for a system consisting of trapped ions, a laser and a detection system is illustrated in Figure 4.6. The induced image charge

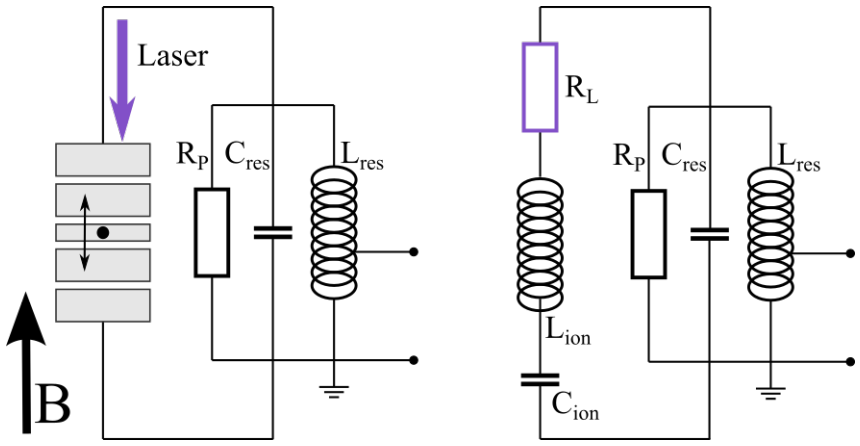

Figure 4.6: Equivalent circuit for the ion-detector-laser interaction. The ion moving up and down in a Penning trap (left) can be modelled as an inductance L_{ion} and capacitance C_{ion} parallel to the resonator circuit (right). The laser acts as a damping force on the ions, equivalent to a series resistance R_L.

current in the electrodes q_{ion} will depend linearly on the ions' deflection for small amplitudes $z(t)$:

$$q_{ion}(t) = \frac{qN}{D} z(t) \quad \Rightarrow \quad I_{ion}(t) = \dot{q}_{ion}(t) = \frac{Nq}{D} \dot{z}(t), \tag{4.12}$$

with a trap specific length D [Brown and Gabrielse, 1986] and the number of trapped particles N. Together with the equation of motion for a trapped ion in thermal equilibrium with the resonator circuit

$$\ddot{z} = -\omega_z^2 z + \frac{Vq}{mD}, \tag{4.13}$$

where V is the voltage at the electrode, the equations can be rewritten in terms of the ion current:

$$V = \frac{mD^2}{Nq^2} \partial_t I(t) + \frac{m\omega_z^2 D^2}{Nq^2} \int I(t) dt \equiv L_{ion} \partial_t I(t) + \frac{1}{C_{ion}} \int I(t) dt. \tag{4.14}$$

This equation of motion equals a linearly damped harmonic oscillator. The comparison to a damped electrical series resonator yields the important parameters:

$$\begin{aligned} C_{ion} &\equiv \frac{Nq^2}{m\omega_z^2 D^2}, \\ L_{ion} &\equiv \frac{mD^2}{Nq^2}, \\ \omega_z &\equiv \frac{1}{\sqrt{L_{ion} C_{ion}}}. \end{aligned} \tag{4.15}$$

The laser acts on the ion like an additional damping force. Therefore, it can be modelled as a resistance R_L in series to the ion:

$$Z_{ion,L} = i\omega L_{ion} - \frac{i}{\omega C_{ion}} + R_L = i\omega R_P \tau \left(1 - \frac{\omega_z^2}{\omega^2}\right) + R_L. \tag{4.16}$$

On resonance, the resonator circuit acts as effective parallel resistance $R_P = \omega L_{res} Q$ with the resonator's inductance L_{res} and the quality factor $Q = \omega_{res}/\Delta\omega$, where $\Delta\omega$ is the full width half maximum of the resonator curve. The cooling time constant $\tau = mD^2/(Nq^2R_P)$ is a measure for the interaction between the ion and the resonator (for the derivation, see appendix B.2). The impedance of the resonator circuit is given by:

$$Z_{RCL} = \left[i\omega C_{res} + \frac{1}{i\omega L_{res}} + \frac{1}{R_P}\right]^{-1} = \frac{R_P}{1 + iQ\left(\frac{\omega}{\omega_{res}} - \frac{\omega_{res}}{\omega}\right)}. \tag{4.17}$$

Using Kirchhoff's laws [Kirchhoff, 1845], the real part of the total impedance is

$$\begin{aligned} Re(Z_{tot}) =& Re\left(\frac{1}{\frac{1}{Z_{ion}} + \frac{1}{Z_{RLC}}}\right) \\ =& \left(\frac{1}{R_P} + \frac{R_L}{R_L^2 + R_P^2\tau^2\omega^2\left(1 - \frac{\omega_z^2}{\omega^2}\right)^2}\right)\left[\left(\frac{1}{R_P} + \frac{R_L}{R_L^2 + R_p^2\tau^2\omega^2(1 - \frac{\omega_z^2}{\omega^2})^2}\right)^2\right. \\ &\left. + \left(\frac{Q\left(\frac{\omega}{\omega_{res}} - \frac{\omega_{res}}{\omega}\right)}{R_P} - \frac{R_P\tau\omega\left(1 - \frac{\omega_z^2}{\omega^2}\right)}{R_L^2 + R_P^2\tau^2\omega^2\left(1 - \frac{\omega_z^2}{\omega^2}\right)^2}\right)^2\right]^{-1}. \end{aligned} \tag{4.18}$$

This is the central building block for the line shape model:

$$\text{dip} = 10log_{10}\left(10^{A/10}Re(Z_{tot})/R_P + C\right), \tag{4.19}$$

giving the dip amplitude in dB for a provided frequency range ω. From fitting this line shape model to a measured dip spectrum, one obtains the center frequency $\omega_z/(2\pi)$ and full width at half maximum $\Delta\nu_z = 1/(2\pi\tau)$ of the dip, the height A and quality factor Q of the resonator, an amplitude offset C, the resonator's resonance frequency $\omega_{res}/(2\pi)$ and most importantly the laser force equivalent resistance R_L.

The number of ions N in the trap follows from the full width at half maximum $\Delta\nu_z$ of the dip

$$N = 2\pi\Delta\nu_z \frac{mD^2}{q^2R_P}. \tag{4.20}$$

Heating and cooling rates

The cooling and heating rates of the beryllium ions due to the laser force depend on the laser detuning from the resonance transition. For a red detuned laser, the beryllium ions moving towards the laser have a higher probability of scattering with a photon than the beryllium ions moving in the opposite direction. The ions are therefore cooled. Conversely, a blue detuned laser heats up the ions. At far detuning, the damping rate of the beryllium ions due to photon scattering is insignificant compared to the coupling to the detector which is given by

$$\gamma_{res} = \frac{1}{2\tau} = \frac{Nq^2 R_P}{2mD^2}. \tag{4.21}$$

The rate of photon absorption R at small ion velocities v is expressed as

$$\begin{aligned} R &= \frac{\Gamma}{2} \frac{S_0}{1 + S_0 + 4\tilde{\delta}^2/\Gamma^2} \\ &\simeq \frac{\Gamma}{2} \frac{S_0}{1 + S_0 + 4\delta^2/\Gamma^2} + \frac{4S_0 k\delta/\Gamma}{\left(1 + S_0 + 4\delta^2/\Gamma^2\right)^2} v + \mathcal{O}(v^2), \end{aligned} \tag{4.22}$$

with the Doppler shifted detuning $\tilde{\delta} = \delta - kv$ from the laser detuning at rest δ, where k is the wave vector. The natural linewidth of the laser-cooling transition is given by $\Gamma = 19.6(10)\,\mathrm{MHz}$ whereas S_0 denotes the saturation of the laser beam with a value between 0 (unsaturated) and 1 (fully saturated). Comparing Eq. (4.22) with a driving and damping force on a particle

$$F_{ion} = \hbar k R_0 - m\gamma_L v \tag{4.23}$$

yields the laser cooling rate γ_L:

$$\gamma_L = -\hbar k^2 4\delta/\Gamma \frac{S_0}{m(1 + S_0 + 4\delta^2/\Gamma^2)^2}. \tag{4.24}$$

This curve is plotted in Figure 4.7. The derivative shows, that most efficient cooling and heating takes place for a laser detuning of $\mp\delta_{max} = \mp\frac{\Gamma}{2}\sqrt{\frac{S_0+1}{3}}$. The laser force equivalent resistance R_L can be translated to a cooling rate by comparison to an ideal resonator (the derivation can be found in the appendix B.2), for which applies

$$\tilde{\gamma}_L = NR_L/(2L_{ion}). \tag{4.25}$$

The notation with the tilde $\tilde{\gamma}_L$ is used to differentiate the laser cooling rate extracted from the dip fit with the equivalent circuit model from the theoretically calculated laser cooling rate γ_L.

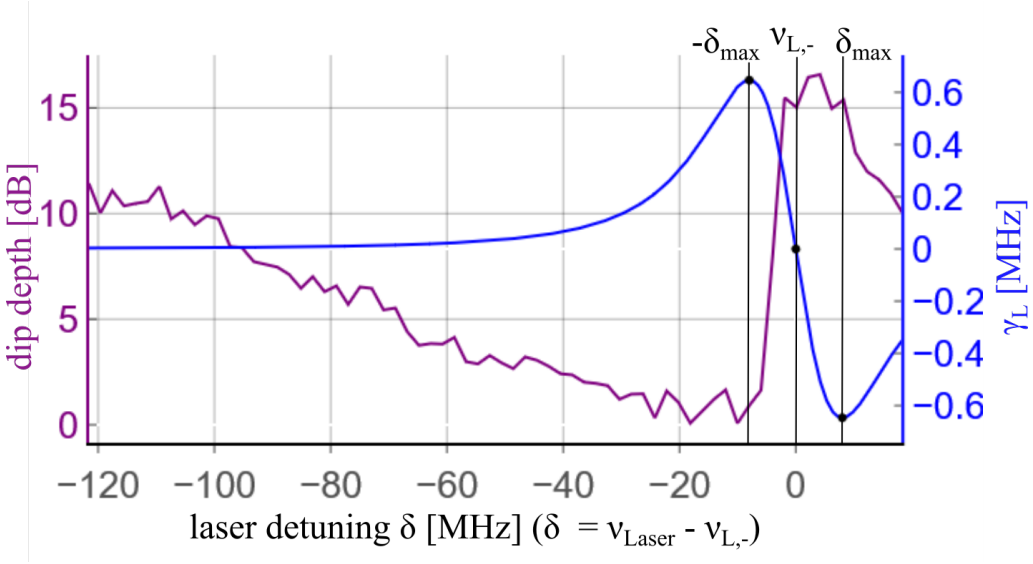

Figure 4.7: Dip depth and laser cooling rate γ_L as function of the laser detuning from the resonance transition $\nu_{L,-}$. As the particles are cooled below the equilibrium temperature with the detector, the dip slowly vanishes. On resonance, the particles are neither heated nor cooled, therefore the dip reappears.Most efficient cooling and heating takes place for a laser detuning of $\mp\delta_{max} = \mp\frac{\Gamma}{2}\sqrt{\frac{S_0+1}{3}}$. For more details, see text. Note that the cooling rate illustrated here for $S_0 = 1$ depends solely on the laser damping force, there is no detector heating included.

4.5 Temperature measurement using dip depth

One indication of laser cooling is the disappearing dip, which signalizes that the temperature of the trapped ions becomes colder than the equilibrium temperature between the ions and the resonator (compare section 4.4). As stated in the previous section, the laser detuning δ from the laser cooling transition frequency $\nu_{L,\pm}$ determines, at which rate γ_L the trapped ions are cooled or heated. Therefore, a scan was performed in which the dip signal was measured for different laser detuning frequencies δ from the lower transition frequency $\nu_{L,-}$. The results are displayed in Figure 4.7. At far detuning, the dip depth approaches the value of 11 dB which is below the maximum dip depth at the transition frequency $\nu_{L,-}$. As the dip depth is an indicator for the temperature discrepancy between beryllium ions and the resonator, this draws the conclusion that without laser cooling, the equilibrium temperature of the beryllium ions is slightly above the resonators temperature.

A few exemplary dip fits are plotted in Figure 4.8 for three laser detunings. From these fits, the dip depth is extracted by subtracting a resonator fit

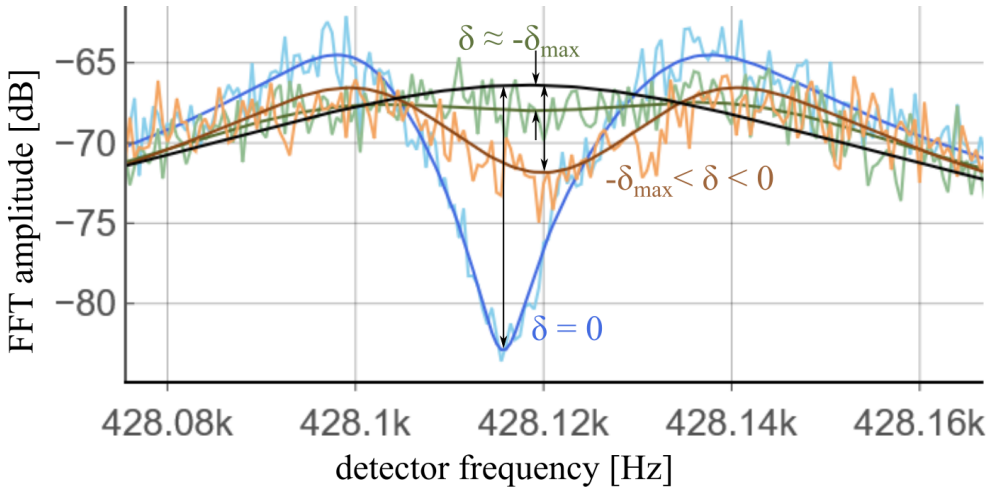

Figure 4.8: Fitted dip signals in the FFT spectrum at different laser detunings for the extraction of the dip depth and the effective laser cooling rate $\tilde{\gamma}_L$. Near the most efficient laser cooling $-\delta_{max}$, the dip becomes very shallow. The maximum dip depth is reached for zero detuning. The arrows indicate the dip depth, which is calculated by subtracting the dip fit from the resonator fit without any particle or laser interaction. On the x-axis, the effective resonator frequency is given with $f_{eff} = f_{res} + f_{DM}$. The used down mix frequency is $f_{DM} = 408.2\,\text{kHz}$.

without any laser and particle interaction from the respective fitted dip signals.

The first parameter, which can be extracted from the scan in Fig. 4.7 is the resonance frequency of the laser cooling transition $\nu_{L,-}$. On resonance, the beryllium ions moving towards the laser beam and the beryllium ions moving away from the laser beam experience the same Doppler shift $\tilde{\delta} = \pm kv$. Hence, the ions are equally cooled and heated, such that the net laser force on the ions is zero. In this case, the beryllium ions are in thermal equilibrium with the resonator and the dip depth is maximal (compare $\nu_{L,-}$ line in Fig. 4.7). For the detuning of $-\delta_{max} = -\frac{\Gamma}{2}\sqrt{\frac{S_0+1}{3}}$, the laser cooling is most efficient and the dip depth becomes minimal. This is also illustrated in Figure 4.7 for a saturated beam $S_0 = 1$. For a larger detuning $-\delta > -\delta_{max}$, the photon absorption rate R decreases which causes the dip depth to increase. On the other side, a positive detuning heats the particle, such that the dip vanishes and eventually turns into a peak. This heating process is shown on the right side of the the resonance frequency. The obtained resonance transition frequency $\nu_{exp} = 957.317\,02\,\text{GHz}$ agrees in the 1.4σ range with the theoretical prediction $\nu_{L,-} = 957.317\,20(13)\,\text{GHz}$.

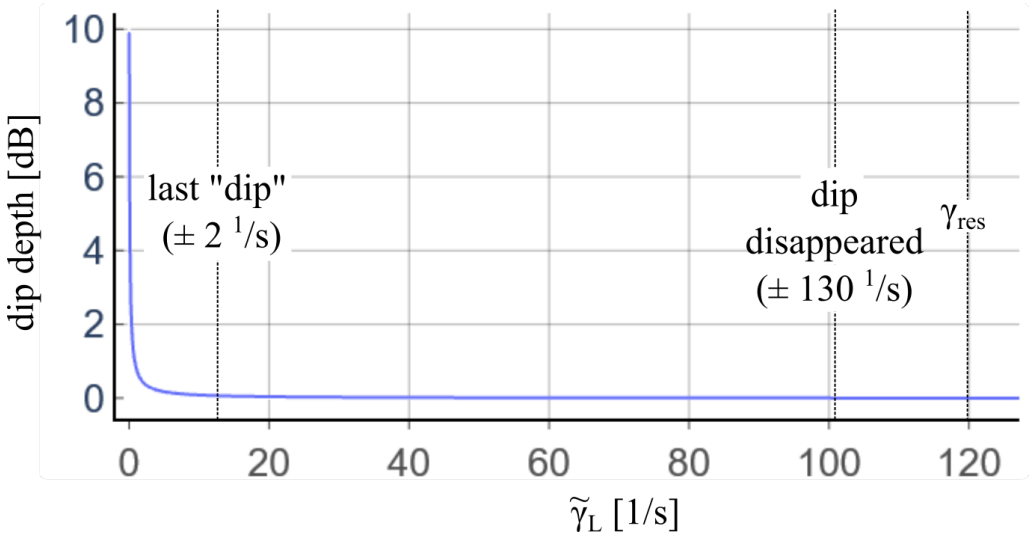

Figure 4.9: Predicted laser cooling rate $\tilde{\gamma}_L$ as function of the dip depth. For very shallow dips, the laser cooling rate $\tilde{\gamma}_L$ is much smaller than the resonator heating rate γ_{res}. However, as soon as the dip disappears, the dip depth extracted from the fit is near zero but varies with the noise of the FFT spectrum. Therefore, $\tilde{\gamma}_L$ varies in a huge range. An upper limit $\tilde{\gamma}_L \geq \gamma_{res}$ can be given once the dip has vanished.

The laser cooling rate $\tilde{\gamma}_L$ is obtained for each laser frequency detuning by fitting the line shape of the dip signal (compare Eq. (4.19) and Eq. (4.25)). The results in Figure 4.10 show cooling rates of up to $\tilde{\gamma}_L \simeq 100(130)\,\mathrm{s}^{-1}$, which is of the same order as the resonator heating rate $\gamma_{res} = 120\,\mathrm{s}^{-1}$. Near the most efficient cooling, the dip vanishes. The errors on $\tilde{\gamma}_L$ become immense and the extracted cooling rates are not reliable anymore. To visualize this problem, Figure 4.9 displays the expected dip depth as function of $\tilde{\gamma}_L$. Near the disappearing dip (dip depth $\simeq 0\,\mathrm{dB}$), the laser cooling rate takes any value from $15\,\mathrm{s}^{-1}$ to infinity. The last (very shallow) dip before the dip fully disappears yields a laser cooling rate of $15(2)\,\mathrm{s}^{-1}$. However, even here the FFT amplitudes of the dip signal feature rms noise of the order of 1.5 dB (compare FFT amplitudes in Figure 4.7). The extracted dip depth hence depends much on the fit and the respective signal. The errors on the fitted laser cooling rate increase with the disappearing dip and once the dip has fully vanished, only an upper limit on the laser cooling rate can be given with $\tilde{\gamma}_L \geq \gamma_{res}$.

From the laser cooling rate $\tilde{\gamma}_L$, a steady-state temperature can be estimated [Bohman et al., 2018]. Considering the energy exchange in the system due to the coupling of the laser and the detector to the beryllium ions with temperatures T_D, T_{res} and T_{Be}, respectively, the steady-state temperature

of the beryllium ions is given by

$$T_{Be} = \frac{\gamma_{res} T_{res} + \tilde{\gamma}_L T_L}{\gamma_{res} + \tilde{\gamma}_L}. \tag{4.26}$$

The temperature calculated for various laser detunings is displayed in Figure 4.10. The dip signal disappears for a laser detuning between roughly $-24\,\mathrm{MHz}$ to $-8\,\mathrm{MHz}$. In this range, no reliable information about the laser cooling rate and hence the temperature can be extracted from fitting the dip line shape. Therefore, the temperature data was fitted for the detunings of $-120\,\mathrm{MHz}$ to $-24\,\mathrm{MHz}$ and extrapolated for detunings beyond using the above Eq. (4.26) and the theoretical cooling rate γ_L in Eq. (4.24) with the free fit parameter being the saturation of the beam S_0:

$$T_{Be} = \frac{\gamma_{res} T_{res} + \gamma_L(S_0) T_L}{\gamma_{res} + \gamma_L(S_0)}. \tag{4.27}$$

According to this fit, a temperature of $4.2\,\mathrm{K}$ was reached with a beam saturation of $S_0 = 1 \times 10^{-4}$. This temperature is far above the calculated Doppler temperature $T_D = 0.47(2)\,\mathrm{mK}$, which is consistent with the small saturation parameter. This is expected: For high temperatures such as the resonator temperature $T_{res} = 10\,\mathrm{K}$, the beam cannot be fully saturated since the Doppler broadening is in the range of a few hundred MHz:

$$\Delta\nu(T_{res}) = \frac{\nu_{Laser}}{c}\sqrt{\frac{8 k_B T_{res} \log 2}{m}} \simeq 720\,\mathrm{MHz}, \tag{4.28}$$

with the speed of light c and the Boltzmann constant k_B. Once the laser cooling starts and the temperature of the system decreases, this also narrows the Doppler broadening which will in turn increase the saturation parameter S_0. The larger S_0, the higher the laser cooling rate and the lower the temperature of the beryllium ions. For a fully saturated beam, an equilibrium temperature of $2.3\,\mathrm{mK}$ is expected for the beryllium ions. Therefore, this fit only gives an upper limit on the ion temperature.

The results will be discussed in section 5.

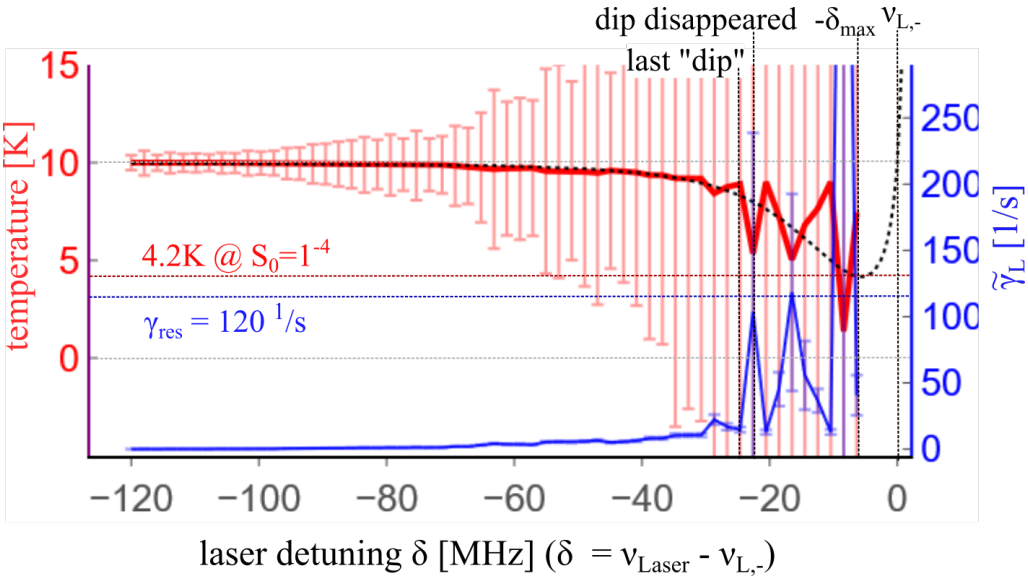

Figure 4.10: Temperature of the cooled beryllium ions and effective laser cooling rate $\tilde{\gamma}_L$ as function of the laser detuning δ. The temperature data was extrapolated (black dashed curve) to estimate an upper limit of the minimum particle temperature $T_{min} \simeq 4.2\,\mathrm{K}$. Due to a large Doppler broadening, the saturation parameter is initially small but is expected to increase with decreasing temperature. However, as soon as the dip disappears, the estimated temperature and laser cooling rate have huge errors, for details see text . The detector temperature was assumed to be $T_D = 10\,\mathrm{K}$.

5 Discussion and outlook

With the direct measurement of the nuclear g-factor of $^3He^{2+}$, He NMR probes for most accurate magnetometry can be established. This enables B-field calibration for other high-precision experiments, amongst others the muon $g-2$ experiment searching for physics beyond the Standard Model [Jegerlehner, 2018]. In addition, QED theory can be tested by comparing the bare helion nuclear g-factor with the recently measured shielded helion nuclear g-factor [Schneider et al., 2022]. High precision in the helion g-factor can be achieved, by measuring the motional eigenfrequencies of a single ion stored in a Penning trap (see chapter 2).

For the helion g-factor measurement, determining the spin-state of the ion is crucial. This is achieved by resolving a spin-flip in an inhomogeneous magnetic field [Dehmelt, 1986], which induces a frequency shift in the axial mode of the ion. Due to it's larger mass and smaller magnetic moment as compared to the proton or electron, the helion's spin-flip induced frequency shift is of the order of background frequency fluctuations (see chapter 2.3). In context of this thesis, two methods to reduce noise in the axial mode for facilitating spin-flip detection were tested.

One major noise contribution in the axial mode originates from the voltage applied to the ring and correction electrodes of the analysis trap. The axial frequency is directly proportional to the square root of the ring voltage (Eq. (2.4)). Therefore, any noise and drift from the voltage source will directly translate into noise and drift in the ion's axial frequency. The requirements for the desired voltage source are high voltage stability (low-noise and low-drift) and tunability over a few hundred mV. To detect a spin-flip with a fidelity of 99 %, the required absolute voltage stability on the correction electrodes is 51 nV, and 23 nV on the ring electrode for a ring voltage of $V_R = -0.43\,\mathrm{V}$. Naturally, this equals a relative voltage stability of 1.2 ppm and 53 ppb for correction and ring electrode, respectively (see section 2.4).

For supplying the ring electrode, the voltage source of choice depends on the required tunability and ring voltage. There are three different options:

The most stable voltage source is based on the inverse Josephson effect [Josephson, 1962] and is nowadays used in metrology for the voltage standard [Behr et al., 2012]. The effect is based on microwave frequency being radiated across a superconducting strip separated by a thin normal conducting layer, called Josephson junction. This leads to steps of constant voltage

[Shapiro, 1963], which scales with the number of junctions in series. The stability of such a Josephson voltage source was measured to be below three parts in 10^{19} [Jain et al., 1987, Tsai et al., 1983]. If the final voltage, which has to be applied to the ring electrode of the analysis trap for detecting the ion, is well known, the highest spin-flip detection fidelity can be reached by directly supplying the ring electrode with the Josephson voltage source. A change in the ion's cyclotron energy shifts the axial frequency (Eq. (2.11)) which evokes the necessity to tune the ring voltage in a range of $\pm 7\,\mathrm{mV}$. This can easily be achieved with the Josephson voltage source which can be tuned in a maximum range of $\pm$ 2.6 % of the output voltage by changing the microwave frequency. If bigger changes in the voltage are needed, the number of junctions in series can be changed. Switching between two different arrays is not a continuous process, but the trap electrodes are set to zero volt in between. Hence, this is only possible if no helion is trapped in the potential created by the Josephson voltage source. For transporting the ion from one trap to another, the Josephson voltage source could be disconnected and replaced by another (less-stable) source using a switch in the room-temperature part of the experiment.

If the needed trap voltage is not well known yet or changes regularly due to e.g. patch potentials on the electrode surface, a larger tunability is needed. Tunability in the range of a few hundred mV can be implemented by adding a low-noise, low-drift DAC in series to the Josephson voltage source. The AD5791 DAC [AD5791, 2022] with a Josephson voltage source as reference voltage contributes $25(3)\,\mathrm{nV}$ noise at an output voltage of $V_{DAC} = 150\,\mathrm{mV}$ (see Fig. 3.9). The typical averaging time is 100 s and is used for all voltage stabilities given hereafter. Such a voltage stability corresponds to a spin-flip detection fidelity of $98^{+1}_{-3}\%$ in the used setup of the helion g-factor measurement. A major advantage of this supply is that the Josephson voltage source can be set to any voltage (depending on the number of Josephson junctions on the chip), while the noise contribution of the DAC remains fixed for $\pm 150\,\mathrm{mV}$ tunability. Thus, it makes no difference in voltage stability whether the composition has an output voltage of $V_R = V_{JJ}(V_{JJ,\mathrm{tune\ MW}}) \pm V_{DAC} = 0.500(13)\,\mathrm{V} \pm 0.15\,\mathrm{V}$ or $V_R = 5.00(13)\,\mathrm{V} \pm 0.15\,\mathrm{V}$. The disadvantage is, that two Josephson voltage sources would be needed: one used as reference voltage for supplying the DAC and the other to set the voltage V_{JJ} for the ring voltage V_R. In a setup where only one Josephson voltage source is used to supply the AD5791 DAC and the DAC is used to set the ring voltage, the voltage stability decreases for increasing DAC output voltage. For example, already at $V_{DAC} = 1\,\mathrm{V}$ the measured stability decreases to 38 nV which corresponds to a spin-flip fidelity of $83^{+4}_{-6}\%$. Another DAC, namely the in-house built StaRep DAC [Böhm et al., 2016], was measured to be less stable (>160 nV) than the AD5791 DAC at $V_{DAC} = 150\,\mathrm{mV}$ using the Josephson voltage source as reference. However, the StaRep DAC was also measured in the workshop of

the Max Planck Institute for Nuclear Physics with the integrated LTZ1000 reference [LTZ, 2022] under perfect conditions (temperature stabilized and no air currents) where the voltage was two times more stable. This suggests, that the StaRep DAC with the Josephson voltage as reference could perform even better in a very stable environment, which is however not a given in the laboratory.

When the required ring voltage is on the order of 0.5 V and tunability is required that exceeds the capabilities of the Josephson voltage source, the best option is to use a commercially available ultra-stable source called UM1-14 [UM, 2022] temperature stabilized to 25 °C. In this source, electronic components are handpicked to acquire high stability. The measured stability 22(3) nV at 500 mV [Bock, 2022] (compare Fig. 3.10) exceeds the stability of the composition of Josephson voltage source plus DAC. Such a stability allows to correctly detect a spin-flip with a probability of $99.2^{+0.4}_{-2.7}\%$. For a higher ring voltage, the UM1-14 stability decreases and the DAC in series to the Josephson voltage source performs better. The UM1-14 can be continuously tuned by pulse width modulation of the internal reference voltage and makes no use of an $R-2R$ ladder. For the correction electrodes which require a lower voltage stability than the ring electrode, the UM1-14 is always suitable.

The second approach to increase the signal-to-noise ratio of an axial frequency shift caused by a spin-flip is concerned with cooling the cyclotron mode to low energy. In an inhomogeneous magnetic field as needed for spin-state detection, the cyclotron mode is coupled to the axial mode (Eq. (2.11)). This leads to noise in the axial mode originating from cyclotron quantum jumps, which decrease with the cyclotron energy [Mooser et al., 2018]. Extremely low energies (or rather temperatures as $E_+ \propto k_B T_+$) in the low mK range can be reached with laser cooled particles. $^3He^{2+}$ does not have a laser cooling transition itself but it can be sympathetically laser cooled as demonstrated in the case of a proton [Bohman et al., 2021] or a highly-charged ion [Tu et al., 2021]. Here, beryllium ions are laser cooled and coupled to the helion. Through energy exchange, the helion's energy is reduced with the cooling of the beryllium ions.

A first indication of laser cooling is the disappearing dip signal: the dip appears for ions which are in thermal equilibrium with the detection system. As the ions' temperature decreases below the detector's temperature, the dip vanishes. The dip depth of a cloud of trapped beryllium ions was measured for different laser detunings, from which the laser cooling rate and eventually an upper limit for the beryllium temperature of 4.2 K could be extracted using an equivalent circuit model (see section 4.4 and 4.5). Assuming a fully saturated beam, a beryllium temperature of 2.3 mK could be reached, as discussed in section 4.5. For a helion coupled via a common resonator to

the beryllium ions, its temperature can be calculated with

$$T_{He} = \frac{T_{res}\gamma_{He} + T_{Be}\tilde{\gamma}_{Be}}{\gamma_{He} + \tilde{\gamma}_{Be}} \quad \text{[Bohman et al., 2021]}. \tag{5.1}$$

The coupling of the beryllium ions to the resonator γ_{res} is reduced in presence of laser cooling to $\tilde{\gamma}_{Be}$ just like the temperature of the beryllium ions T_{Be} decreases with laser cooling. The resonator temperature T_{res} is approximately 10 K and the helion coupling to the detector is given by $\gamma_{He} = R_P 4e^2/(2m_{He}D^2) = 42$ Hz. An upper limit of the helion temperature is estimated using $T_{Be} = 4.2$ K and $\tilde{\gamma}_{Be} = \gamma_{res} = 119$ Hz. The reached helion axial temperature for a common resonator coupling on resonance would be $T_{He,z} = 5.7$ K. Likewise, for a beryllium temperature of $T_{Be} = 2.3$ mK, an axial temperature of $T_{He,z} = 2.6$ K can be reached. This corresponds to a helion cyclotron temperature of 896 K and 409 K (Eq. (4.2)), respectively. This temperature is far from the mK range needed for high fidelity spin-state detection. Once the beryllium temperature T_{Be} becomes sufficiently smaller than the resonator's temperature (around 8 K), the dip vanishes and the extracted information from the dip fit becomes extremely imprecise and unreliable. In addition, lower temperatures are reached if the ions are detuned from the resonance frequency of the detection system [Tu et al., 2021].

Other temperature measurement techniques are more conclusive. For example for a single helion, the Boltzmann distribution of the cyclotron energy (and therefore the cyclotron temperature) can be extracted from the axial frequency measurement in the analysis trap $\nu_z(E_+)$ using Eq. (2.11) [Bohman, 2020]. In another approach, the laser frequency is swept over the entire beryllium cooling resonance while the fluorescent photons are registered. The width of the fluorescence spectrum is related to the axial temperature via the Doppler width $\Delta f_{FWHM} = f_0/c \cdot \sqrt{2k_B T/m}$. Then, the cyclotron temperature of the helion is determined from the coupling between helion and beryllium and between helion and resonator. This method unfortunately did not work in the scope of this thesis, as the fluorescent photons could not be resolved (see section 4.3). For the future setup, apertures will be installed to reduce background photons. This might also diminish the charging of the trap electrodes due to ambient photons, which constantly changed the ion's eigenfrequencies in the used setup (even the magnetron frequency was shifted once the UV laser was sent through the trap tower). To mention a third method, the helion's axial temperature also follows a Boltzmann distribution, which can be mapped out by adding an inhomogeneity ($C_4 \neq 0$) to the trapping potential [Egl, 2020]. In such a potential, the axial temperature scales with the radius of the axial motion in phase-space. By exciting the helion in the axial mode and alternatively sympathetically cooling it, the thermal distribution of radii is observed from

which T_z is obtained.

The next step in the $^3He^{2+}$ g-factor measurement will be to attach the Josephson voltage source directly to the ring electrode of the analysis trap. By observing the axial frequency fluctuations of a trapped ion, the stability of this voltage source is measured with higher sensitivity than at the nanovoltmeter. Also, the combination of Josephson voltage source and a DAC in series for tunability will be tested directly on the Penning-trap setup.

In terms of the sympathetic laser-cooling scheme, the integration of apertures in front of the trap chamber will reduce stray light from the laser beam. This enables a temperature measurement based on the detection of fluorescent photons, which will be tested in the future setup. Since the setup is also used for hyperfine structure measurements [Schneider et al., 2022] which requires the transmission of microwaves through the trap chamber, these apertures have to be permeable for microwaves. The 1 mm PVC apertures built in-house with a thickness of 2 mm were tested to transmit microwaves while at the same time the laser beam profile stays gaussian.

Also upcoming is the sympathetic cooling of $^3He^{2+}$. For the coupling of the helion to the beryllium ions, different methods will be tested. Apart from the common resonator coupling discussed in the results section 4.5, the ions can be coupled via a common endcap [Tu et al., 2021]. In addition, a new coupling trap is currently in fabrication, which allows the direct coupling of the ions exploiting the Coulomb force.

A Lists

A.1 List of Figures

A.2 List of Tables

B Further information

B.1 Josephson voltage source

Operating instructions for the Josephson voltage source

When working with Josephson voltage sources, a few things have to be considered:

- Before inserting the Josephson voltage source into the cryogenic tank, one has to make sure the chip is dry. Ice on the surface could lead to damage of the Josephson array.
- When slowly inserting the Josephson voltage source into liquid helium, no cables should be connected. Otherwise, currents could inhibit partial sections of the array to become superconductive.
- Once cool, the voltage readout cables and subsequently the current supply cables can be attached. Cable pairs should be twisted to avoid ground loops. Preferably, the microwave synthesizer is also mounted after the junctions have cooled down.
- Now, the 0^{th} step can be controlled on the oscilloscope. By turning on the microwave synthesizer, the step width should slightly decrease.
- The power source must be switched off before reconnecting or switching devices. Omission can lead to flux (non-superconducting parts in the array).
- The microwave synthesizer has a frequency dependant power output. Hence, for non-symmetric steps, especially if one flank is steep whereas the other is rounded, the microwave power has to be adapted.
- If the Shapiro steps feature a slope, normally conducting parts are present. To resolve this, the junctions have to be heated up (the microwave is turned off and all cables have to be detached). Once the whole chip is normally conducting, the junction can be cooled down again.

From experience, measurements can be carried out successfully if these points are considered and if additionally the array is properly grounded.

Arrays of the Josephson voltage source

number of junctions	connection
4096	1
2048	2
1024	3
512	4
256	5
128	6
1	7
1	8
2	9
4	10
8	11
16	12
32	13
64	14
	22

Table B.1: Arrays of Josephson junctions and the respective connection on a SUB-D25.

B.2 Laser

Derivation of the laser cooling rate:

The voltage drop in the series RLC circuit is given by:

$$V = L_{ion}\partial_t I(t) + I(t)R_L + \frac{1}{C_{ion}}\int I(t)dt, \tag{B.1}$$

compare Equation 4.14. The derivative with respect to the current leads to the differential equation

$$0 = \frac{d^2I(t)}{dt^2} + \frac{R_L}{L}\frac{dI(t)}{dt} + \frac{1}{LC}I(t) \equiv \ddot{I} + 2\tilde{\gamma_L}\dot{I} + \omega_z I, \tag{B.2}$$

which is solved for

$$I(t) = A\exp\left(-\frac{R_L}{2L}t\right) \tag{B.3}$$

by identifying $R_L = 2\sqrt{L/C}$. The prefactor in the exponent determines the damping of the RLC circuit which is equivalent to the coupling between the ion and the resonator $\tilde{\gamma_L} = \frac{R_L}{2L}N$. The N appears, as the cooling rate is independent of the number of particles in the trap whereas L is proportional to the number of particles.

Derivation of the detector cooling rate:

The image current induced by a number of N particles in an electrode is given by

$$I_{ind} = \frac{qN}{D}\dot{z} \tag{B.4}$$

which produces a voltage drop

$$V = R_P I_{ind}. \tag{B.5}$$

Inserting V into Equation (4.13) yields the differential equation

$$\begin{aligned} \ddot{z} &= -\omega_z^2 z + \frac{Vq}{mD} = -\omega_z^2 z + \frac{R_P q^2 N}{mD^2}\dot{z}, \\ \Leftrightarrow 0 &= \ddot{z} + 2\gamma_{res}\dot{z} + \omega_z^2 z \end{aligned} \tag{B.6}$$

from which the detector cooling rate follows:

$$\gamma_{res} = \frac{R_P q^2 N}{2mD^2}. \tag{B.7}$$

Shifts of Be energy levels in presence of a magnetic field:

state	m_J	m_I	$\Delta\nu$
$^2S_{1/2}$	$+1/2$	$-3/2$	80.579 GHz
	$+1/2$	$-1/2$	80.302 GHz
	$+1/2$	$+1/2$	80.023 GHz
	$+1/2$	$+3/2$	79.743 GHz
	$-1/2$	$+3/2$	-79.642 GHz
	$-1/2$	$+1/2$	-79.989 GHz
	$-1/2$	$-1/2$	-80.335 GHz
	$-1/2$	$-3/2$	-80.680 GHz
$^2P_{3/2}$	$+3/2$	$+3/2$	160.276 GHz
	$+3/2$	$+1/2$	160.243 GHz
	$+3/2$	$-1/2$	160.211 GHz
	$+3/2$	$-3/2$	160.178 GHz
	$+1/2$	$+3/2$	53.460 GHz
	$+1/2$	$+1/2$	53.426 GHz
	$+1/2$	$-1/2$	53.392 GHz
	$+1/2$	$-3/2$	53.358 GHz
	$-1/2$	$+3/2$	-53.357 GHz
	$-1/2$	$+1/2$	-53.392 GHz
	$-1/2$	$-1/2$	-53.426 GHz
	$-1/2$	$-3/2$	-53.461 GHz
	$-3/2$	$+3/2$	-160.173 GHz
	$-3/2$	$+1/2$	-160.209 GHz
	$-3/2$	$-1/2$	-160.245 GHz
	$-3/2$	$-3/2$	-160.281 GHz

Table B.2: Beryllium energy level shifts of all hyperfine levels in $^2S_{1/2}$ and $^2P_{3/2}$. The signs denote the shift due to a B-field of 5.720 611 8 T relative to the non-shifted energy level.

C Bibliography

AD5791. Data sheet: AD5791 DAC Analog Devices, 2022. URL https://www.analog.com/media/en/technical-documentation/data-sheets/ad5791.pdf.

David W Allan and James A Barnes. A modified "Allan variance" with increased oscillator characterization ability. 1981.

T Andersen, KA Jessen, and G Sørensen. Mean-life measurements of excited electronic states in neutral and ionic species of beryllium and boron. *Physical Review*, 188(1):76, 1969.

AOM. Data sheet: Acousto-optical modulator Gooch and Housego, 2022. URL http://www.hanamuraoptics.com/laseroptics/Gooch&Housego/I-M110-3C10BB-3-GH27.pdf.

Collaboration ATLAS et al. A particle consistent with the higgs boson observed with the atlas detector at the large hadron collider. *Science*, 338(6114):1576–1582, 2012.

Ralf Behr, Oliver Kieler, Johannes Kohlmann, Franz Müller, and Luis Palafox. Development and metrological applications of Josephson arrays at PTB. *Measurement Science and Technology*, 23(12):124002, 2012. ISSN 0957-0233. doi: 10.1088/0957-0233/23/12/124002. URL https://iopscience.iop.org/article/10.1088/0957-0233/23/12/124002.

Maik Biroth, Patrick Achenbach, Werner Lauth, and Andreas Thomas. Performance of sensl C-series SiPM with high photoelectron resolution at cryogenic temperatures. In *2016 IEEE Nuclear Science Symposium, Medical Imaging Conference and Room-Temperature Semiconductor Detector Workshop (NSS/MIC/RTSD)*, pages 1–3, 2016. doi: 10.1109/NSSMIC.2016.8069771.

Klaus Blaum. High-accuracy mass spectrometry with stored ions. *Physics Reports*, 425(1):1–78, 2006. ISSN 0370-1573. doi: 10.1016/j.physrep.2005.10.011. URL https://www.sciencedirect.com/science/article/pii/S0370157305004643.

Nils Vincent Bock. Bachelor thesis: Modellierung einer Penning-Falle zur Nutzung sympathetischer Laserkkühlung und Charakterisierung dafür geeigneter Spannungsquellen, 2022.

M. Bohman, A. Mooser, G. Schneider, N. Schön, M. Wiesinger, J. Harrington, T. Higuchi, H. Nagahama, C. Smorra, S. Sellner, K. Blaum, Y. Matsuda, W. Quint, J. Walz, and S. Ulmer. Sympathetic cooling of protons and antiprotons with a common endcap penning trap. *Journal of Modern Optics*, 65(5-6):568–576, 2018. doi: 10.1080/09500340.2017.1404656.

M. Bohman, V. Grunhofer, C. Smorra, M. Wiesinger, C. Will, M. J. Borchert, J. A. Devlin, S. Erlewein, M. Fleck, S. Gavranovic, J. Harrington, B. Latacz, A. Mooser, D. Popper, E. Wursten, K. Blaum, Y. Matsuda, C. Ospelkaus, W. Quint, J. Walz, and S. Ulmer. Sympathetic cooling of a trapped proton mediated by an LC circuit. *Nature*, 596(7873): 514–518, 2021. ISSN 1476-4687. doi: 10.1038/s41586-021-03784-w. URL https://www.nature.com/articles/s41586-021-03784-w#citeas.

Matthew Bohman. Dissertation: Sympathetic cooling of a proton with resonant image current coupling, 2020.

Bollinger, Wells, Wineland, and Itano. Hyperfine structure of the 2p 2p1/2 state in 9Be+. *Physical review. A, General physics*, 31(4):2711–2714, 1985. ISSN 0556-2791. doi: 10.1103/PhysRevA.31.2711.

Lowell S. Brown and Gerald Gabrielse. Precision spectroscopy of a charged particle in an imperfect Penning trap. *Phys. Rev. A*, 25(4):2423–2425, 1982. doi: 10.1103/PhysRevA.25.2423. URL https://link.aps.org/doi/10.1103/PhysRevA.25.2423.

Lowell S. Brown and Gerald Gabrielse. Geonium theory: Physics of a single electron or ion in a Penning trap. *Rev. Mod. Phys.*, 58(1):233–311, 1986. doi: 10.1103/RevModPhys.58.233. URL https://link.aps.org/doi/10.1103/RevModPhys.58.233.

Ch. Böhm, S. Sturm, A. Rischka, A. Dörr, S. Eliseev, M. Goncharov, M. Höcker, J. Ketter, F. Köhler, D. Marschall, J. Martin, D. Obieglo, J. Repp, C. Roux, R.X. Schüssler, M. Steigleder, S. Streubel, Th. Wagner, J. Westermann, V. Wieder, R. Zirpel, J. Melcher, and K. Blaum. An ultra-stable voltage source for precision penning-trap experiments. *Nuclear Instruments and Methods in Physics Research Section A: Accelerators, Spectrometers, Detectors and Associated Equipment*, 828:125–131, 2016. ISSN 0168-9002. doi: https://doi.org/10.1016/j.nima.2016.05.044. URL https://www.sciencedirect.com/science/article/pii/S0168900216304259.

Chin-Wen Chou, David B Hume, Till Rosenband, and David J Wineland. Optical clocks and relativity. *Science*, 329(5999):1630–1633, 2010.

CODATA. Codata values of the fundamental constants, 2022. URL https://physics.nist.gov/cgi-bin/cuu/Category?view=html&All+values.x=49&All+values.y=11.

H. Dehmelt. Continuous Stern-Gerlach effect: Principle and idealized apparatus. *Proceedings of the National Academy of Sciences of the United States of America*, 83(8):2291–2294, 1986. ISSN 0027-8424. doi: 10.1073/pnas.83.8.2291.

Wolfgang Demtröder. *Laserspektroskopie 2: Experimentelle Techniken*. Springer Berlin Heidelberg, Berlin, Heidelberg, 6. aufl. 2013 edition, 2013. ISBN 9783642214479. URL http://nbn-resolving.org/urn:nbn:de:bsz:31-epflicht-1515685.

Oriol Domènech, Alex Pomarol, and Javi Serra. Probing the standard model with dijets at the lhc. *Physical Review D*, 85(7), 2012. ISSN 1550-7998. doi: 10.1103/PhysRevD.85.074030.

Alexander Egl. Dissertation: High-precision laser spectroscopy of the fine structure in 40ar13+ at ALPHATRAP, 2020.

FLUKE. Data sheet: AD5791 DAC Analog Devices, 2022. URL https://eu.flukecal.com/category/obsolete/obsolete-products/8508a-85-digit-reference-multimeter?quicktabs_product_details=2.

G. Gabrielse. Why is sideband mass spectrometry possible with ions in a Penning trap? *Physical review letters*, 102(17):172501, 2009. ISSN 0031-9007. doi: 10.1103/PhysRevLett.102.172501.

G. Gabrielse, L. Haarsma, and S. L. Rolston. Open-endcap Penning traps for high precision experiments. *International Journal of Mass Spectrometry and Ion Processes*, 88(2):319–332, 1989. ISSN 0168-1176. doi: 10.1016/0168-1176(89)85027-X. URL https://www.sciencedirect.com/science/article/pii/016811768985027X.

Ingolf Volker Hertel and Claus-Peter Schulz. *Atome, Moleküle und optische Physik 1: Atomphysik und Grundlagen der Spektroskopie*. Springer-Lehrbuch. Springer Berlin Heidelberg, Berlin, Heidelberg, 2015. ISBN 9783662468081. URL http://nbn-resolving.org/urn:nbn:de:bsz:31-epflicht-1547515.

HighFinesse. Data sheet: HighFinesse wavelength meter WS-8, 2022. URL https://www.highfinesse.com/en/wavelengthmeter/wavelengthmeter-ws-8-2.html.

Jonathan P. Home, David Hanneke, John D. Jost, Jason M. Amini, Dietrich Leibfried, and David J. Wineland. Complete methods set for scalable ion trap quantum information processing. *Science*, 325(5945):1227–1230, 2009. doi: 10.1126/science.1177077. URL https://www.science.org/doi/abs/10.1126/science.1177077.

Jain, Lukens, and Tsai. Test for relativistic gravitational effects on charged particles. *Physical review letters*, 58(12):1165–1168, 1987. doi: 10.1103/physrevlett.58.1165.

F. Jegerlehner. The muon g-2 in progress, 2018. URL https://arxiv.org/pdf/1804.07409.

B. D. Josephson. Possible new effects in superconductive tunnelling. *Physics Letters*, 1(7):251–253, 1962. ISSN 00319163. doi: 10.1016/0031-9163(62)91369-0.

Keysight. Keysight 3458A data sheet, 2022. URL https://docs.rs-online.com/0789/A700000006556902.pdf.

Studiosus Kirchhoff. Ueber den Durchgang eines elektrischen Stromes durch eine Ebene, insbesondere durch eine kreisförmige. *Annalen der Physik*, 140(4):497–514, 1845. ISSN 1521-3889. doi: 10.1002/andp.18451400402. URL https://onlinelibrary.wiley.com/doi/10.1002/andp.18451400402.

Johannes Kohlmann and Ralf Behr. Development of Josephson voltage standards. In Adir Moyses Luiz, editor, *Superconductivity*. IntechOpen, 2011. ISBN 978-953-307-151-0. doi: 10.5772/17031.

Lasertex. Data sheet: HeNe frequency laser standard, 2022. URL https://lasertex.eu/products/frequency-laser-standard/.

Litron. Data sheet: Nd:YAG laser, 2022. URL https://litron.co.uk/wp-content/uploads/2022/05/Litron-Nano-Brochure-Apr-22.pdf.

LTZ. Data sheet: LTZ1000 ultra precision reference - Linear Technology, 2022. URL https://www.analog.com/media/en/technical-documentation/data-sheets/LTZ1000.pdf.

A. Mooser, H. Kracke, K. Blaum, S. A. Bräuninger, K. Franke, C. Leiteritz, W. Quint, C. C. Rodegheri, S. Ulmer, and J. Walz. Resolution of single spin flips of a single proton. *Physical review letters*, 110(14):140405, 2013. doi: 10.1103/PhysRevLett.110.140405.

A. Mooser, S. Ulmer, K. Blaum, K. Franke, H. Kracke, C. Leiteritz, W. Quint, C. C. Rodegheri, C. Smorra, and J. Walz. Direct high-precision measurement of the magnetic moment of the proton. *Nature*,

509(7502):596–599, 2014. ISSN 1476-4687. doi: 10.1038/nature13388. URL https://www.nature.com/articles/nature13388.

A. Mooser, A. Rischka, A. Schneider, K. Blaum, S. Ulmer, and J. Walz. A new experiment for the measurement of the g -factors of 3 He + and 3 He 2+. *Journal of Physics: Conference Series*, 1138:012004, 2018. ISSN 1742-6588. doi: 10.1088/1742-6596/1138/1/012004.

Andreas Mooser. *Der g-Faktor des Protons*. PhD thesis, Johannes Gutenberg-Universität Mainz, 2014.

Franz Müller, Thomas J. Scheller, Jinni Lee, Ralf Behr, Luis Palafox, Marco Schubert, and Johannes Kohlmann. Microwave design and performance of PTB 10 V circuits for the programmable Josephson voltage standard. *World Journal of Condensed Matter Physics*, 04(03):107–122, 2014. ISSN 2160-6919. doi: 10.4236/wjcmp.2014.43016. URL https://www.scirp.org/journal/paperinformation.aspx?paperid=48805.

Anna Nikiel, Peter Blümler, Werner Heil, Manfred Hehn, Sergej Karpuk, Andreas Maul, Ernst Otten, Laura M. Schreiber, and Maxim Terekhov. Ultrasensitive 3he magnetometer for measurements of high magnetic fields. *The European Physical Journal D*, 68(11), 2014. ISSN 1434-6060. doi: 10.1140/epjd/e2014-50401-3.

F. Paschen and E. Back. Normale und anomale Zeemaneffekte. *Annalen der Physik*, 344(15):897–932, 1912. ISSN 1521-3889. doi: 10.1002/andp.19123441502.

Mariusz Puchalski and Krzysztof Pachucki. Fine and hyperfine splitting of the 2P state in Li and Be+. *Physical Review A*, 79(3), 2009. ISSN 1050-2947. doi: 10.1103/PhysRevA.79.032510.

William Riley and David A. Howe. Handbook of frequency stability analysis. 2008. URL https://www.nist.gov/publications/handbook-frequency-stability-analysis.

Adam Rudziński, Mariusz Puchalski, and Krzysztof Pachucki. Relativistic, qed, and nuclear mass effects in the magnetic shielding of 3he. *The Journal of chemical physics*, 130(24):244102, 2009. doi: 10.1063/1.3159674.

P. O. Schmidt, T. Rosenband, C. Langer, W. M. Itano, J. C. Bergquist, and D. J. Wineland. Spectroscopy using quantum logic. *Science*, 309 (5735):749–752, 2005. doi: 10.1126/science.1114375. URL https://www.science.org/doi/abs/10.1126/science.1114375.

A. Schneider, B. Sikora, S. Dickopf, M. Müller, N. S. Oreshkina, A. Rischka, I. A. Valuev, S. Ulmer, J. Walz, Z. Harman, C. H. Keitel, A. Mooser,

and K. Blaum. Direct measurement of the 3he+ magnetic moments. *Nature*, 606(7916):878–883, 2022. ISSN 1476-4687. doi: 10.1038/s41586-022-04761-7.

Antonia Schneider. *Design of theAnalysis Trap and He Ion Source for the 3He2+ magnetic moment measurement: Master*. PhD thesis, Ruprecht-Karls-Universität Heidelberg, 2019. URL https://pure.mpg.de/pubman/faces/ViewItemOverviewPage.jsp?itemId=item_3050281.

Georg Schneider, Andreas Mooser, Matthew Bohman, Natalie Schön, James Harrington, Takashi Higuchi, Hiroki Nagahama, Stefan Sellner, Christian Smorra, Klaus Blaum, Yasuyuki Matsuda, Wolfgang Quint, Jochen Walz, and Stefan Ulmer. Double-trap measurement of the proton magnetic moment at 0.3 parts per billion precision. *Science (New York, N.Y.)*, 358 (6366):1081–1084, 2017. doi: 10.1126/science.aan0207.

Sidney Shapiro. Josephson currents in superconducting tunneling: The effect of microwaves and other observations. *Physical review letters*, 11 (2):80–82, 1963. ISSN 0031-9007. doi: 10.1103/physrevlett.11.80.

SiPM. Data sheet: SiPM onsemi array j-series, 2022. URL https://www.onsemi.com/pdf/datasheet/arrayj-series-d.pdf.

C. Smorra, S. Sellner, M. J. Borchert, J. A. Harrington, T. Higuchi, H. Nagahama, T. Tanaka, A. Mooser, G. Schneider, M. Bohman, K. Blaum, Y. Matsuda, C. Ospelkaus, W. Quint, J. Walz, Y. Yamazaki, and S. Ulmer. A parts-per-billion measurement of the antiproton magnetic moment. *Nature*, 550(7676):371–374, 2017. ISSN 1476-4687. doi: 10.1038/nature24048. URL https://www.nature.com/articles/nature24048?date=2018-09-05&e=3&url=wwin-tv.com.

Sven Sturm. *The g-factor of the electron bound in 28Si13+*. PhD thesis, Ruprecht-Karls-Universität Heidelberg, 2011.

Sven Sturm, Günter Werth, and Klaus Blaum. Electron g -factor determinations in penning traps. *Annalen der Physik*, 525(8-9):620–635, 2013. ISSN 1521-3889. doi: 10.1002/andp.201300052.

TOPTICA. Data sheet: DLC TA-FHG pro, 2022. URL https://www.toptica.com/fileadmin/Editors_English/11_brochures_datasheets/03_Short_Info/toptica-ta-shg-fhg-short-info.pdf.

Jaw-Shen Tsai, A. K. Jain, and J. E. Lukens. High-precision test of the universality of the Josephson voltage-frequency relation. *Physical review letters*, 51(4):316–319, 1983. ISSN 0031-9007. doi: 10.1103/physrevlett.51.316.

Bingsheng Tu, Felix Hahne, Ioanna Arapoglou, Alexander Egl, Fabian Heiße, Martin Höcker, Charlotte König, Jonathan Morgner, Tim Sailer, Andreas Weigel, Robert Wolf, and Sven Sturm. Tank–circuit assisted coupling method for sympathetic laser cooling. *Advanced Quantum Technologies*, 4(7):2100029, 2021. ISSN 2511-9044. doi: 10.1002/qute.202100029.

Stefan Ulmer, Klaus Blaum, and Wolfgang Quint. *Trapped charged particles: A graduate textbook with problems and solutions.* Advanced textbooks in physics. World Scientific, New Jersey and London and Singapore and Beijing and Shanghai and Hong Kong and Taipei and Chennai and Tokyo, 2016. ISBN 978-1-78634-011-5.

UM. Data sheet: UM1-14 ultra precision reference - Stahl Electronics, 2022. URL https://www.stahl-electronics.com/bilder/Manual_UM_LN_SW_V2017.pdf.

D. J. Wineland, J. J. Bollinger, and Wayne M. Itano. Laser-fluorescence mass spectroscopy. *Physical review letters*, 50(9):628–631, 1983. ISSN 0031-9007. doi: 10.1103/PhysRevLett.50.628.

ZurichInstruments. Data sheed: Lock-in amplifier, 2022. URL https://docs.zhinst.com/uhf_user_manual/overview.html.

Declaration:

I, Annabelle Valerie Kaiser (matriculation number 3480878), hereby declare that I have produced the work presented in this thesis, during the scheduled period of study. I also declare that I have not taken any material from any source except referred to.

Heidelberg, August 3, 2022 _____

Danksagung:

An dieser Stelle möchte ich mich herzlich bei allen bedanken, die mich während meiner Zeit hier am MPIK unterstützt haben und zum Gelingen dieser Masterarbeit beigetragen haben.

Lieber Klaus, ich bin geehrt dass Du auf mich zugekommen bist um mir ein Praktikum in Deiner Abteilung anzubieten - und das in einer Zeit, in der sich andere Arbeitsgruppen von der Außenwelt abgeschottet haben. Deine Begeisterung und Motivation sind ansteckend und es hat mir große Freude bereitet, hier auch für die Masterarbeit bleiben zu dürfen. Deine gelegentlichen Besuche im Büro oder Labor, um über die Arbeit und das Leben im Allgemeinen zu quatschen, waren bereichernd und zeugen von Deinem großen Interesse am Wohlergehen Deiner Abteilungsmitglieder. Das Arbeitsklima hier ist hervorragend und stellt die besten Voraussetzungen für eine erfolgreiche Promotion. Danke auch für das Korrekturlesen und die konstruktiven Kommentare! Ich freue mich auf die zukünftigen Gespräche, Kicker-Tourniere und Gruppenausflüge.

Lieber Andi, herzlichen Dank, dass Du mich in Deiner wunderbaren Gruppe aufgenommen hast! Du hast mir mit unglaublicher Geduld bei meinen Problemen geholfen und immer guten Ideen zum Gelingen der Projekte beigetragen, an denen ich gerade gearbeitet habe. Du hattest immer ein offenes Ohr für Fragen, hast Dir meine Probevorträge angehört und im Büro für gute Laune gesorgt. Herzlichen Dank für das Korrekturlesen und die Kommentare, die mich zum Weiterschreiben und Verbessern motiviert haben!

Ein riesiges Dankeschön, an die Gruppenmitglieder des 3-Helium Experiments Stefan, Marius, Ute, Nils und Philipp für die tolle Arbeitsgemeinschaft und die Gespräche beim Mittagessen. Lieber Stefan, Du bist in jeder Situation ein hervorragender Ansprechpartner und auf Dein überragendes Gedächtnis und Dein faszinierendes Wissen ist Verlass. Du hast Dir selbstlos Zeit genommen um mir beim Programmieren, Laser optimieren oder anderen Labortätigkeiten zu helfen und hast mir geduldig physikalische Zusammenhänge erklärt. Lieber Marius, mit Dir kann man einfach am besten Helium füllen und Du standest mir stets mit Rat und Tat in allen technischen Belängen zur Seite. Auch Deine bewundernswerte Art, Kuchen und andere Süßspeisen zu vernichten und Deine Besuche zum Quatschen im Büro haben mir immer Freude bereitet. Besonders glücklich bin ich über den Wanderausflug an der Zugspitze - vielen Dank Euch beiden für die Idee, Beförderung und das unglaubliche Erlebnis.

Auch bei allen Pentatrappern (u.a. Kathrin, Menno, Alex, Daniel, Jost) und Alphatrappern (u.a. Jonathan, Charlotte und Tim) möchte ich mich herzlich bedanken! Mit Euch und den 3-Helium Leuten kann man nicht nur beim Mittagessen Spaß haben, sondern auch am Danteplatz bei einem Bierchen plaudern oder am Ehrenfriedhof auf der Mauer den Abend ausklingen lassen. Euer Teamgeist fängt einen auch an Tagen auf, an denen im Labor wirklich nichts funktioniert. Ein besonderer Dank geht an Menno für die Unterstützung bei Messungen mit der Josephson junction.

Lieber Luis und lieber Ralf, in dem einwöchigen Praktikum an der PTB habe ich nicht nur viel gelernt, sondern auch viel Spaß gehabt. Ihr habt Euch beide viel Zeit für mich genommen und das Labor mit guter Laune und norddeutschem Humor gefüllt. Es war ein Privileg, mit Euch zusammenzuarbeiten und die kulinarischen Highlights in Braunschweig zu erkunden, vielen Dank für alles.

A big thanks to you, Yuri, for being the second referee of my master thesis! Herzlichen Dank auch an Dominik, Dennis und Thomas für die Hilfe bei Messungen mit der StaRep und die Bereitstellung von allen möglichen elektrischen Teilen. Liebe Gabi, vielen Dank für die Organisation von Gruppenausflügen, den MATS-Tagen auf Schloss Ringberg und Deine Unterstützung bei Reiseanträgen. Dein Organisationstalent ist bewundernswert und es macht immer Spaß, sich mit Dir zu unterhalten.

Liebe Mama, lieber Papa, liebe Oma Rose, Opa Dieter, Oma Ursel und Opa Ernst, Ihr habt mich auf das Leben vorbereitet und mir das Studium ermöglicht. Eure unentwegte Unterstützung und Glauben an mich sind Gold wert, dafür möchte ich mich herzlich bedanken.

Zu guter Letzt ein fettes Merci an meine Mitbewohnerinnen Teresa und Raissa und an Jonas - ihr wart tagtäglich für mich da, habt mich unterstützt und für eine grandiose Work-Life Balance gesorgt. Ich werde die gemeinsamen Gespräche, Gin Tastings, Koch Aktionen und die schönen Ausflüge vermissen!